gels

MDPI

Article

Copper-/Zinc-Doped TiO_2 Nanopowders Synthesized by Microwave-Assisted Sol–Gel Method

Luminița Predoană [1], Gabriela Petcu [1], Silviu Preda [1,*], Jeanina Pandele-Cușu [1], Simona Viorica Petrescu [1], Adriana Băran [1], Nicoleta G. Apostol [2], Ruxandra M. Costescu [2], Vasile-Adrian Surdu [3], Bogdan Ştefan Vasile [3] and Adelina C. Ianculescu [3]

[1] Institute of Physical Chemistry "Ilie Murgulescu" of the Romanian Academy, 202 Splaiul Independenței, 060021 Bucharest, Romania
[2] National Institute of Materials Physics, Atomiștilor 405A, 077125 Măgurele, Romania
[3] Department of Science and Engineering of Oxide Materials and Nanomaterials, Faculty of Chemical Engineering and Biotechnologies, "Politehnica" University of Bucharest, 1–7 Gh. Polizu, 011061 Bucharest, Romania
* Correspondence: predas@icf.ro

Abstract: Using the microwave-assisted sol–gel method, Zn- and Cu-doped TiO_2 nanoparticles with an anatase crystalline structure were prepared. Titanium (IV) butoxide was used as a TiO_2 precursor, with parental alcohol as a solvent and ammonia water as a catalyst. Based on the TG/DTA results, the powders were thermally treated at 500 °C. XRD and XRF revealed the presence of a single-phase anatase and dopants in the thermally treated nanoparticles. The surface of the nanoparticles and the oxidation states of the elements were studied using XPS, which confirmed the presence of Ti, O, Zn, and Cu. The photocatalytic activity of the doped TiO_2 nanopowders was tested for the degradation of methyl-orange (MO) dye. The results indicate that Cu doping increases the photoactivity of TiO_2 in the visible-light range by narrowing the band-gap energy.

Keywords: copper-/zinc-doped TiO_2 powders; microwave-assisted sol–gel method; thermal behavior; photocatalytic activity

check for updates

Citation: Predoană, L.; Petcu, G.; Preda, S.; Pandele-Cușu, J.; Petrescu, S.V.; Băran, A.; Apostol, N.G.; Costescu, R.M.; Surdu, V.-A.; Vasile, B.Ș.; et al. Copper-/Zinc-Doped TiO_2 Nanopowders Synthesized by Microwave-Assisted Sol–Gel Method. *Gels* **2023**, *9*, 267. https://doi.org/10.3390/gels9040267

Academic Editors: Yulong Zhang and Hui-Juan Xu

Received: 10 February 2023
Revised: 17 March 2023
Accepted: 22 March 2023
Published: 23 March 2023

Copyright: © 2023 by the authors. Licensee MDPI, Basel, Switzerland. This article is an open access article distributed under the terms and conditions of the Creative Commons Attribution (CC BY) license (https://creativecommons.org/licenses/by/4.0/).

1. Introduction

Environmental pollution constitutes a problem around the world, and scientists are working to achieve new or improved methods and materials to reduce such pollutants. The photocatalytic degradation of pollutants in the environment or water using solar radiation is the most used method today [1–3].

Nanosized TiO_2-based materials are known as the most important photocatalyst for environmental applications. These materials are intensively studied for their advantages such as their nontoxicity, higher activity, lower price, and chemical and photoresist properties [4–6]. Among the three polymorphs (anatase, brookite, and rutile) of TiO_2, anatase has the best photocatalytic activity [7,8].

A major influence on the properties of the final product is the preparation method. The current trend is to replace methods that use mechanical force (high-energy consumption and long preparation time) with gentle chemical methods (soft chemistry). By using soft chemical methods, a better control over the purity and stoichiometry of the studied metal oxides can be achieved [8–10].

Undoped or doped titanium-dioxide powders were obtained by different methods. Among them, the most frequently used methods in the liquid phase are: the sol–gel process [11–16], hydrothermal methods [8,17], coprecipitation [18], hydrothermal-assisted sol–gel method [19], microwave-assisted hydrothermal method [20,21], ultrasound-assisted sol–gel [18,22], and microwave-assisted sol–gel [19,23–25].

The sol–gel method presents advantages such as: synthesis at low temperatures and the use of simple and accessible technological equipment, the realization of materials with a clearly defined arrangement that can be controlled by the type of precursors used in the synthesis, and low cost by optimizing the energy cost and creating products with different shapes [15,18].

In recent research works, the microwave-assisted sol–gel method has received special interest for the preparation of oxide materials [26,27]. Microwave synthesis combines the advantage of speed and homogeneous heating of the precursor materials by making it possible to homogeneously heat the reaction solution by using microwave irradiation during the preparation process. The micro- and macroscopic characteristics of oxide materials, such as shape and morphology, defects of the surface area, purity, particle size, and reaction kinetics were improved by using microwave irradiation [28].

In the case of the sol–gel method, the hydrolysis and polycondensation reactions are complex and occur simultaneously. By the sol–gel method, powders or gels can be obtained, depending on the pH of the solution, which can be regulated by using catalysts. By microwave irradiation of the sol–gel solution, monodisperse nanoparticles are obtained (fast nucleation in a supersaturated solution) [29].

Up to now, numerous studies have been reported TiO_2 materials prepared with different methods and modifications such as doping, heterojunction formation, nanocomposites, etc., for photocatalytic degradation applications [30–33]. Titanium dioxide is one of the most used semiconductors in photocatalytic applications due to its advantageous properties, such as cost effectiveness, ecofriendly nature, photostability, chemical inertness, and high stability, but it has a high band gap-energy value (around 3.2 eV) that limits its use only to the UV range [34]. Increasing TiO_2 activity efficiency under the visible light range is one of the most desired improvements, and a facile way to accomplish that is by TiO_2 modification with metal or nonmetal elements. Thus, intermediate energy levels are created by the dopants which reduce the band gap of TiO_2 [35]. Furthermore, a better separation of electron–hole pairs is obtained by providing new sites that capture photogenerated electrons, leading to an increase in photocatalytic efficiency [36]. The effective mass of photogenerated electron–hole pairs, as well as the mobility and diffusibility of the photoexcited charge carriers, can be determined by the dopant and vacancy band shapes (charge-separation efficiency) [37]. Metals, such as Cu and Zn, are suitable for TiO_2 doping in order to improve photocatalytic performance [34,38,39], presenting interest in this field due to their relative abundancy and low costs [34,40]. Although there are many reports in the literature regarding TiO_2 doped with copper or zinc, there is still interest in optimizing the synthesis method in order to obtain materials with improved properties. Compared to the other synthesis methods (Table 1), the microwave-assisted sol–gel route has advantages over several properties of synthesized materials such as small size and homogeneity of the particle, high crystallinity, controlled morphology, and high purity [41]. All these properties of the materials obtained, controlled by choosing the optimal synthesis conditions, ultimately influenced the photocatalytic activity, as can be observed in Table 1.

Table 1. Comparative results reported in the literature on methyl-orange photocatalytic degradation in the presence of Cu- or Zn-doped TiO_2 obtained by different methods.

Preparation Method	Dopant Content	Irradiation-Light Type	Methyl-Orange Concentration	Degradation Efficiency, [%]	Ref.
		Cu-doped TiO_2			
sol–gel method	TiO_2−Cu 2.0%	UV and visible light	1×10^{-5} M	97% UV 16% Vis	[35]
hydrothermal process (180 °C for 8 h)	0, 2, 4, 6, 8, and 10% Cu-TiO_2	simulated sunlight irradiation (300 W Xe lamp)	20 mg/L	87.7% of MO (3 cycles, 6% Cu-TiO_2) Photocatalytic degradation efficiencies of MO: 6% Cu-TiO_2 > 4% Cu-TiO_2 > 8% Cu-TiO_2 > 2% Cu-TiO_2 > 10% Cu-TiO_2 > TiO_2	[42]
TiO_2 by sol–gel method; [Cu(OHCor)]/TiO_2 composite by reflux	[Cu(OHCor)]/TiO_2	visible white LED lamp of 30 W	10 ppm	31.0%@2.5 h for TiO_2 79.5% for [Cu(OH-Cor)]/TiO_2 Decrease by 5.7% ([Cu(OH-Cor)]/TiO_2 after 3 cycles	[43]
hydrothermal method (220 °C for 24 h)	Fe_3O_4@TiO_2 1 wt%, 2 wt% and 3 wt% Cu-Fe_3O_4@TiO_2	sunlight illumination	20 mg/L	85%@2.5 h for MO for Fe_3O_4@TiO_2 85%@2.5 h for MO for 3 wt% Cu-Fe_3O_4@TiO_2	[44]
sol–gel method	TiO_2 Cu/TiO_2 rFA/Cu/TiO_2 oxide Acid- FA/Cu/TiO_2 Base- FA/Cu/TiO_2	UVA (λ = 365 nm); visible light (Opple, 4.5 W)	10 ppm	81.8% UV, 6.7% Vis for TiO_2 37.4% UV, 15.3% Vis for Cu/TiO_2 79% UV 58.8% Vis for rFA/Cu/TiO_2 100% UV and 99.1%% Vis for Base-FA/Cu/TiO_2 96.9% UV for Acid-FA/Cu/TiO_2	[45]
solvothermal method	TiO_2 0.1 mol%Cu-TiO_2 0.3 mol%Cu-TiO_2 Cu/N-TiO_2 0.5 mol%Cu-TiO_2 1 mol%Cu-TiO_2	simulated visible light (250 W hydrogen lamp, 464 nm)	20 mg/L	94.3% after 8 cycles for Cu/N-TiO_2 Cu/N-TiO_2 is four times better than TiO_2 (reaction rate constant 0.695 h^{-1})	[46]
one-step solvothermal synthesis method	TiO_2-RGO TiO_2-RGO-xCuO (x = 0.05, 0.075, 0.1, 0.3, 0.5%)	simulated visible light (250 W neon lamp, 464 nm)	20 ppm	94.8% after 8 cycles for TiO_2-RGO-0.075%CuO	[47]
sol–gel method	TiO_2 Cu/TiO_2 (1:1 wt%) Cu/TiO_2/FA	UVA (λ = 365 nm); visible light (Opple, 4.5 W)	5, 15, 25, or 100 ppm	54.32% for Cu/TiO_2 (visible) 11.59% for TiO_2 (visible) 89.53% for TiO_2 (UV) 70.27% for Cu/TiO_2 (UV) 96.78% for Cu/TiO_2/FA (UV) 89.54% for Cu/TiO_2/FA (Visible)	[48]

Table 1. *Cont.*

Preparation Method	Dopant Content	Irradiation-Light Type	Methyl-Orange Concentration	Degradation Efficiency, [%]	Ref.
hydrothermal synthesis method (24 h at 200 °C)	TiO_2 TiO_2/Cu OPMTC (Organic porous materials-TiO_2/Cu composite)	simulated sunlight (a); nature sunlight (b)	100 mg/L	55.8% (a), 49.1% (b) 91.8% (a), 86.5% (b) 96.3% (a), 92.6% (b)	[49]
in situ approach	AA AA-0.5Cu AA-1Cu AA-1.5Cu AA-5Cu AA-10Cu P25 P25-0.5Cu P25-1Cu P25-1.5Cu P25-5Cu P25-10Cu	UV-A (6 × 6 W fluorescence lamp, 365 nm)	1 g L^{-1}	75.6% 7.1% 6.6% 14.5% 17.4% 23.1% 82.8% 37.5% 38.1% 30.5% 24.9% 39.1%	[50]
hydrothermal	Cu	UV	10 ppm	90% in 150 min	[51]
		Zn-doped TiO_2			
sol–gel method	TiO_2 − Zn 2.0%	UV and visible light	1 × 10^{-5} M	90% UV 30% Vis	[35]
Micro-arc oxidation, impregnation	MAO (TiO_2) MAOZn (Zn-TiO_2)	UV (250 W, 365 nm)	5 mg·L^{-1}, 10mg·L^{-1}, 15mg·L^{-1} and 20 mg·L^{-1}	94% MAOZn films 90% after 10 cycles	[52]
sol–gel reflux synthesis route	Zn (3 mol %)-TiO_2 Zn (5 mol %)-TiO_2	UV-A (1.29 mW cm^{-2}, 466 nm)	1 mg of dye in 100 mL H_2O	95.6% for MO 99.6% for MO	[53]
sol–gel route	Ag,Zn-TiO_2	solar simulator (100 LCL Compact Xenon Light lamp)	4 ppm	58.5% at pH 11 84.4% at pH 2.1, 2 gL^{-1} catalyst dose 93.1% at pH 4.1, 2 gL^{-1} catalyst dose Complete mineralization at 8 gL^{-1} catalyst dose within 60 and 120 min for Ag–Zn-TiO_2	[54]
simple coprecipitation method	TZO-4 (ZnO/TiO_2)	UV (500 W, λ max = 365 nm)	20 mg/L	99%/90 min	[55]
stearic-acid-gel method; sol–gel method	P25 $(0, 0.05, 0.1, 0.3, 0.5, 1)_{ste}$ Zn-TiO_2 0.1_{sol} Zn-TiO_2 At 400, 450, 500 and 600 °C	mercury lamp (300 W)	20 mg/l	0.1% Zn/$TiO_{2\ ste}$—best photodegradation of the dye 0.1% Zn/$TiO_{2\ ste}$ > 0.1% Zn/$TiO_{2\ sol}$ > P25 For 0.1%Zn/$TiO_{2\ ste}$ series 450 °C > 400 °C > 500 °C > 600 °C	[56]

Table 1. *Cont.*

Preparation Method	Dopant Content	Irradiation-Light Type	Methyl-Orange Concentration	Degradation Efficiency, [%]	Ref.
ligand exchange reaction and with additional thermal treatment	Pure TiO_2 metal oxide TiO_2(-Zn) TiO_2(-Zn)+HCl	UV light reactor (400 W high-pressure mercury lamp)	20 mg/l	Residual MO 0.799 mg/L@1h, 0.637 mg/L@2h and 0.528 mg/L@3h for metal oxide TiO_2(-Zn) 0.859 mg/L@1h, 0.748 mg/L@2h and 0.685 mg/L@3h for pure TiO_2 0.742 mg/L@1h, 0.542 mg/L@2h and 0.403 mg/L@3h for TiO_2(-Zn)+HCl	[57]
ligand exchange reaction and with additional thermal treatment	TiO_2 nanotubes $Zn(acac)_2$ assembled TiO_2 nanotubes	UV light reactor (400 W high-pressure mercury lamp)	20 mg/L	Residual MO in $Zn(acac)_2$ assembled TiO_2 nanotubes At 300 °C 19.72 mg/L@1h, 19.08 mg/L@2 h and 18.24 mg/L@3 h At 400 °C 13.82 mg/L@1 h, 9.44 mg/L@2h and 7.02 mg/L@3 h At 500 °C 15.32 mg/L@1 h, 12.70 mg/L@2 h and 10.82 mg/L@3 h Zn ions surface-doped TiO_2 nanotubes > Pure TiO_2 nanotubes > pure TiO_2 nanoparticles	[58]

The aim of this work was to obtain photocatalytic materials with improved properties that would be active under visible light for the degradation of organic pollutants from wastewater by a simple and cost-effective method. Thus, in the present paper, Cu- and Zn-doped TiO_2 powders were prepared by the microwave-assisted sol–gel method in a basic medium. The influence of the synthesis method and dopant on the structure and the photocatalytic properties of these materials were evaluated. The TiO_2-based nanopowders were used for the degradation of methyl-orange (MO) organic dye in order to evaluate the potential of these materials for environmental applications.

2. Results and Discussion

The samples were investigated following their thermal behavior, morphology, and structure, and their photocatalytic properties. In the case of the TiO_2-Cu 2.0% MW sample, a white-green amorphous powder was obtained, while for the TiO_2-Zn 2.0% MW sample, the obtained powder was amorphous and had a white color.

2.1. As-Prepared Samples

2.1.1. SEM Results

SEM analysis was performed in order to investigate the morphology of the as-prepared samples, and the micrographs are shown in Figure 1.

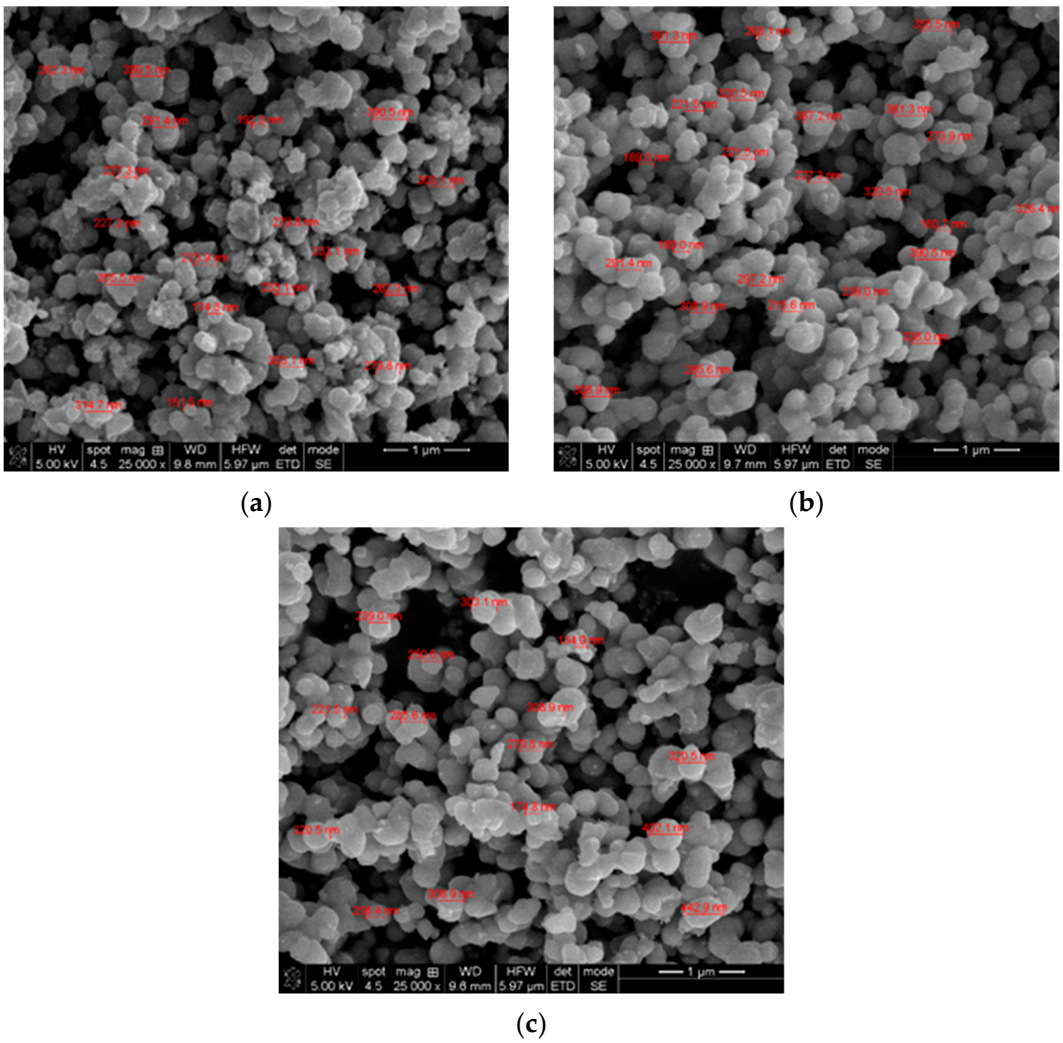

Figure 1. SEM micrographs of the as-prepared samples; (**a**) TiO_2 MW, (**b**) TiO_2-Cu 2.0% MW, (**c**) TiO_2-Zn 2.0% MW.

According to the morphological observation, the size and shape of the as-prepared samples are similar, without any noticeable differences. However, in case of the TiO_2 MW sample (Figure 1a), the nanoparticles surfaces appear to be quasi-irregular with jagged edges, while for the doped ones, the profile is well-defined.

2.1.2. Thermal Behavior

The thermal stability of the samples was estimated using TG/DTG/DTA analysis. The thermograms indicate the physical and/or chemical changes that occur in the samples during heat treatment. Figure 2a,b depicts the temperature-dependent mass curves of the TiO_2−Cu 2.0% MW (Figure 2a) and TiO_2−Zn 2.0% MW (Figure 2b) samples. During the whole measurement, the TiO_2−Cu 2.0% MW sample exhibited a total mass loss of −16.85%, which can be further separated into three mass-loss steps of −11.62%, −4.89%, and −0.34%. The TiO_2−Zn 2.0% MW sample showed a total mass loss of −18.58%, corresponding to three mass-loss steps of −13.91%, −4.13%, and −0.54%. The origin of the mass-loss step below 200 °C is most probably the release of physisorbed water and alcohols from the samples. Following this fact, the thermal effect on the DTA curve, corresponding to the mass loss, had the peak located at 91 °C for the TiO_2−Cu 2.0% MW sample, and at 93 °C for the TiO_2−Zn 2.0% MW sample, respectively.

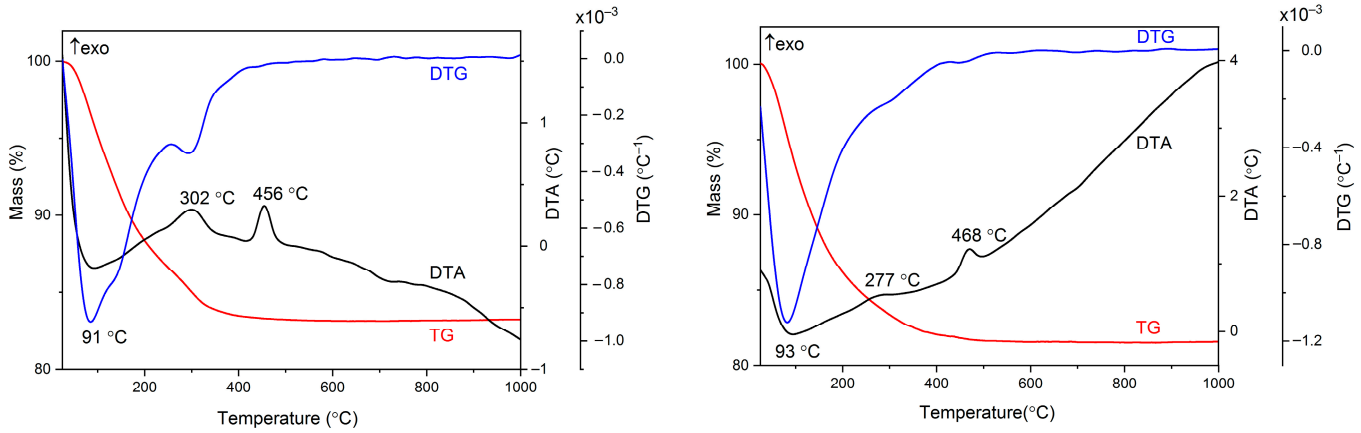

Figure 2. The TG (red)/DTG (blue)/DTA (black) curves of the (**a**) TiO_2−Cu 2.0% MW sample and (**b**) TiO_2−Zn 2.0% MW sample; heating rate was 10 °C/min, using air as carrier gas.

The second mass loss, which ranged from 200 °C to 400 °C, was most probably due to the decomposition of the residual organic groups and partial dehydroxylation of $Ti(OH)_4$. The thermal effect associated with the second mass loss is an exothermic effect centered at 302 °C for the TiO_2−Cu 2.0% MW sample, and 277 °C for the TiO_2−Zn 2.0% MW sample, respectively, as previously reported for a similar alkoxide precursor [59–61]. The dehydroxylation of $Ti(OH)_4$ is an event that takes place over a wide temperature range and continues up to 500 °C, leading to the transformation from an amorphous phase to crystalline anatase. The second exothermic effect, located at 456 °C for the TiO_2−Cu 2.0% MW sample, and 468 °C for the TiO_2−Zn 2.0% MW sample, respectively, without corresponding to mass loss on the TG curve, suggests complete dehydroxylation and anatase crystallization [62,63].

2.1.3. XPS on the As-Prepared Samples

To verify the oxidation state of each element, all the sample surfaces were investigated by XPS. In the following section, we will discuss the as-prepared samples. All the core-level spectra of interest (Ti 2p, O 1s, Zn 2p, Cu 2p) were analyzed using Voigt profiles, as described in ref. [64]. The integral areas obtained by the deconvolution procedure were normed to the atomic-sensitivity factors provided by ref. [65]. The binding energies were

corrected such that the C value was 284.6 eV. Aside from the photoelectron emission peaks, XPS spectra can also show the presence of Auger electrons (emitted when an outer shell electron fills the photoelectron vacancy following core ionization).

The XPS spectra and their deconvolutions are illustrated in Figures 3–6. The peaks for Ti 2p, O 1s, Zn 2p, and Cu 2p were attributed as described in Table 2 and revealed the presence of different species such as Ti(IV), Zn(II), and Cu(I), consistent with the database [66–68]. The Ti 2p doublet has a spin-orbit splitting of 5.71 eV, which supports the presence of Ti(IV). If we take into consideration the total intensity of each element, we obtain TiO_2 with different percentages of dopants, as depicted in Table 2.

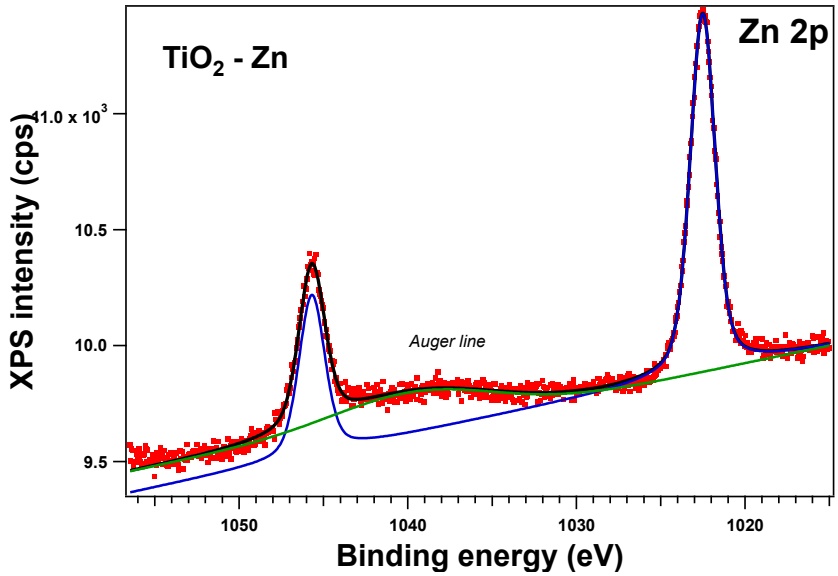

Figure 3. XPS spectra of the Zn 2p level of the as-prepared Zn-doped sample: red symbols for the experimental data, black line for the fit, blue line for C1, and green line for C2 (Auger line).

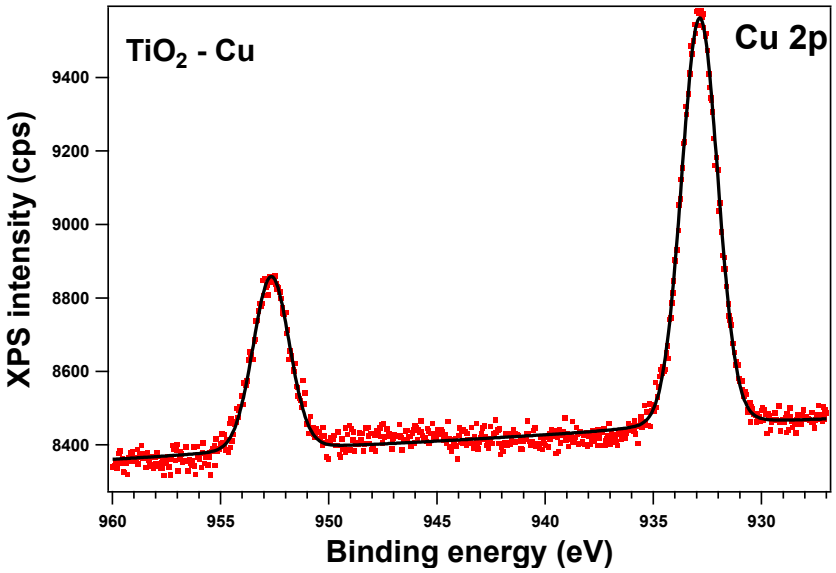

Figure 4. XPS spectra of the core level Cu 2p of the as-prepared Cu-doped sample: red symbols for the experimental data and black line for the one-component fit.

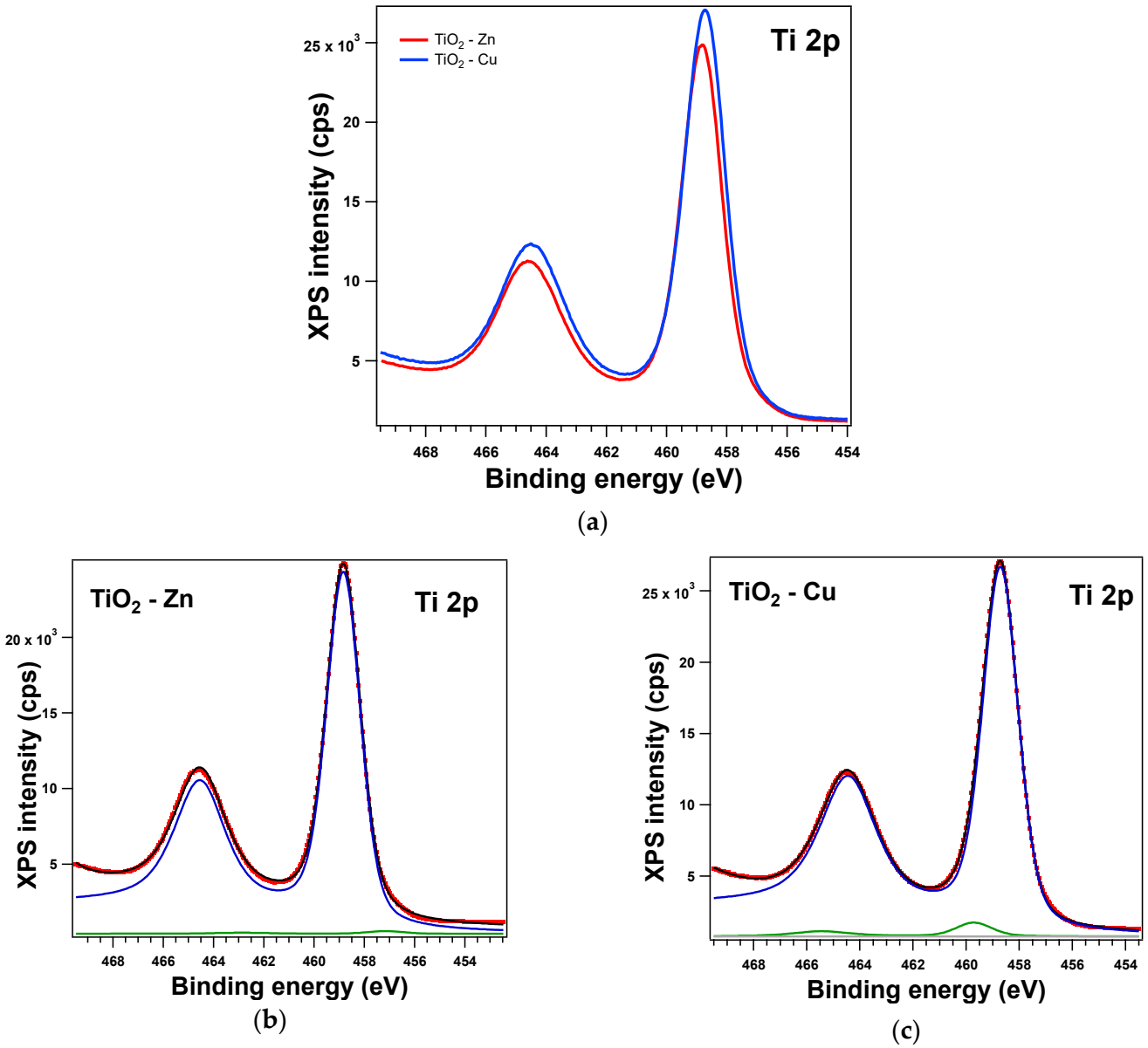

Figure 5. XPS spectra of the Ti 2p level: (**a**) comparison between the experimental data: red line for Zn-doped samples and blue line for the Cu-doped samples, and (**b**,**c**) the fit and deconvolutions for the Zn sample and Cu sample, respectively: red symbols for the experimental data overlayed with a black line for the fit, blue line for C1, and green line for C2.

2.2. Thermally Treated Samples

2.2.1. SEM Results

The surface morphology of the thermally treated powders, obtained by SEM, are illustrated in Figure 7.

Analogous to the previously investigated untreated samples, the micrographs reveal uniformly distributed nanoparticles with the formation of aggregated clusters with similar shapes and sizes for the TiO_2 MW sample compared to doped ones. Because of the agglomeration of the particles, no specific shapes could be determined, as previously reported [69].

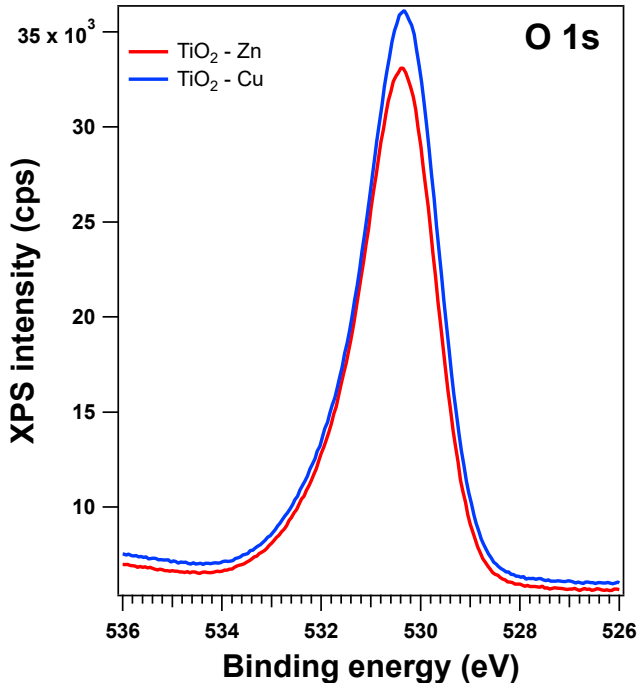

(**a**)

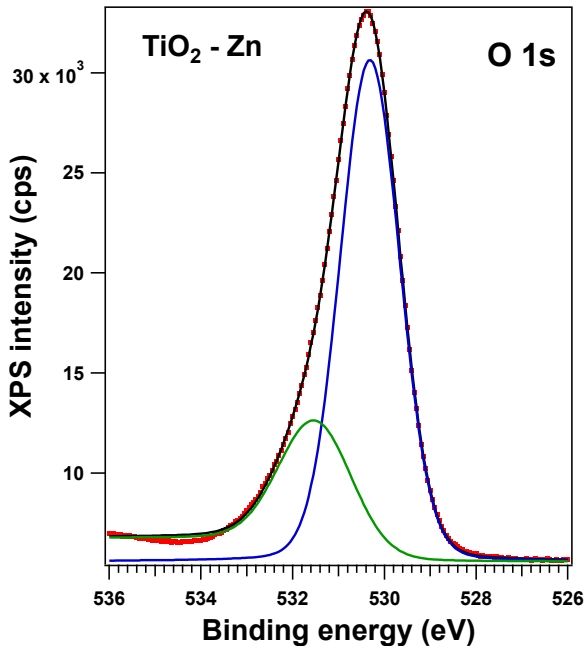

(**b**)

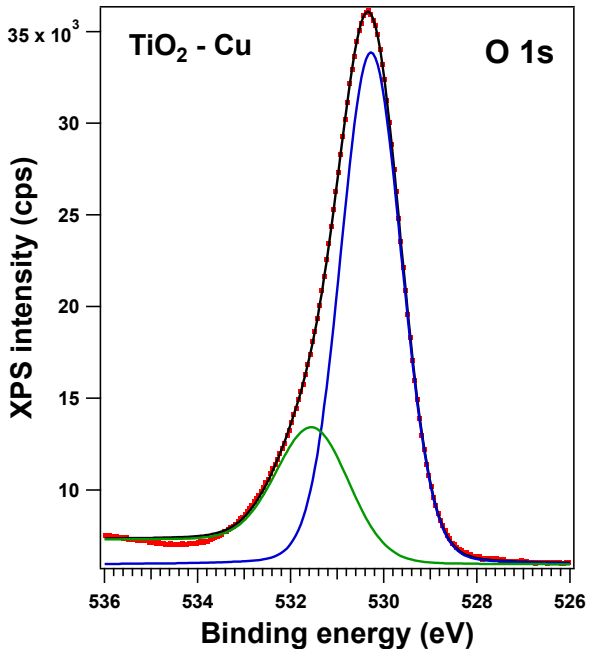

(**c**)

Figure 6. XPS spectra of the O 1s level: (**a**) experimental data for the Zn (red line)- and Cu (blue line)-doped samples and red symbols for the experimental data overlayed with a black line for the fit and deconvolutions for (**b**) the Zn sample and (**c**) the Cu sample: blue line for C1 and green line for C2.

Table 2. Binding energies (BE), atomic %, and attributions of the deconvolutions for the core levels for the as-prepared samples.

	Element		BE (eV)	% at	Interpretation
TiO_2-Zn 2.0% MW	Ti 2p	C1	457.15	0.25	Ti(IV) vol.
		C2	458.82	32.59	Ti(IV) surf.
				32.84	
	O1s	C1	530.32	50.71	Ti(IV)
		C2	531.49	15.9	TiO_2/TiO_x + Zn(II) + cont
				66.61	
	Zn $2p_{3/2}$	C1	1022.52	0.55	Zn(II)
					$TiO_{2.03}$—Zn 0.55%
TiO_2-Cu 2.0% MW	Ti 2p	C1	458.70	32.58	Ti(IV) vol.
		C2	459.71	1.26	Ti(IV) surf.
				33.84	
	O1s	C1	530.28	51.02	Ti(IV)
		C2	531.50	14.75	TiO_2/TiO_x + Zn(II) + cont
				65.77	
	Cu $2p_{3/2}$	C1	932.86	0.39	Cu(I)
					TiO_2—Cu 0.39%

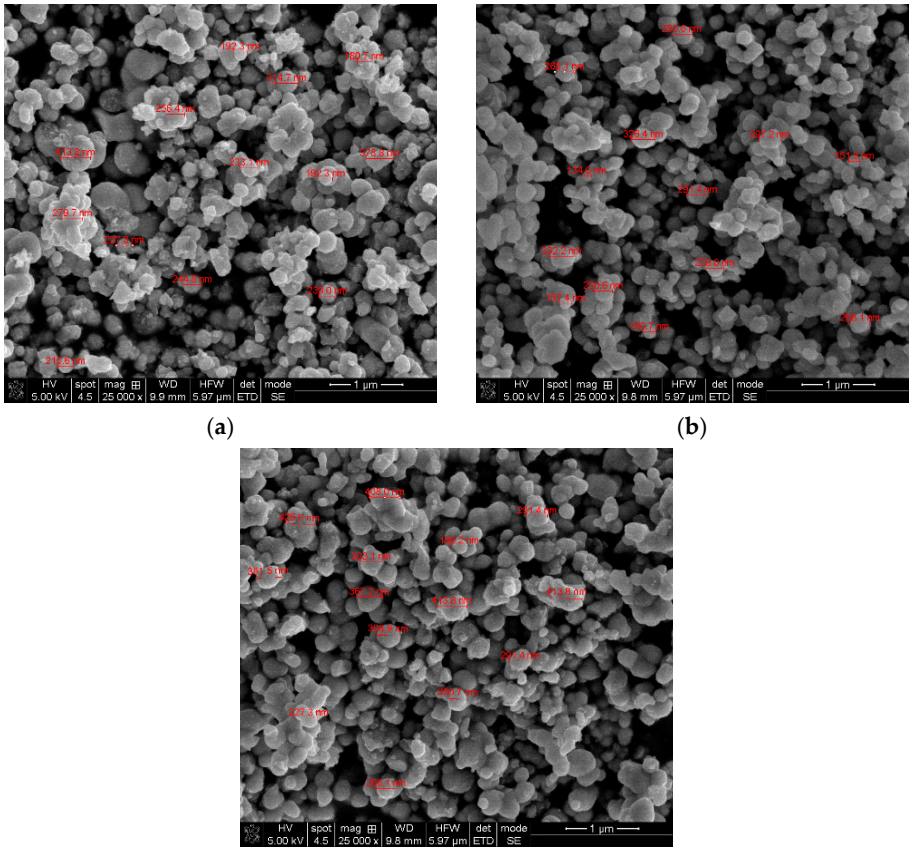

(**a**) (**b**)

(**c**)

Figure 7. SEM micrographs of the thermally treated samples; (**a**) TiO_2 MW, (**b**) TiO_2−Cu 2.0% MW, (**c**) TiO_2−Zn 2.0% MW.

2.2.2. XRD Results

Figure 8 displays the diffractograms of the undoped TiO_2 sample, thermally treated at 450 °C, and Zn- and Cu-doped TiO_2 samples, thermally treated at 500 °C, respectively. All diffraction lines correspond to the TiO_2 anatase phase, according to ICDD file no. 21−1272. No polymorphs of titanium oxide (rutile or brookite) or Cu- and Zn-based compounds were detected within the limit of the instrument. This observation suggests that the dopants enter the anatase structure or are distributed on the anatase particle surface in the form of tiny clusters [70]. To determine the impact of Cu and Zn dopants (2% molar) on the anatase structure, the lattice parameters, crystallite size, and microstrain were calculated, and the results are listed in Table 3.

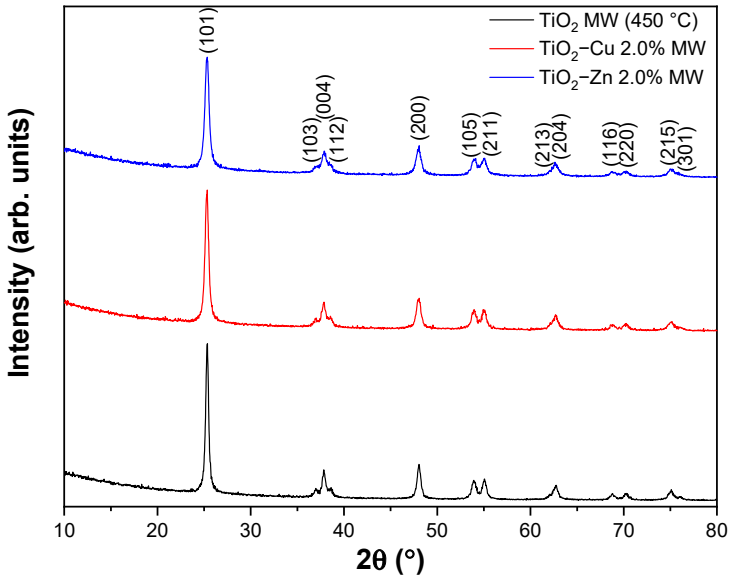

Figure 8. X–ray diffraction patterns of microwave-assisted sol–gel prepared samples, thermally treated (bottom—undoped TiO_2 sample, middle—Cu-doped TiO_2 sample, and top—Zn-doped TiO_2 sample).

Table 3. The lattice parameters, the estimated crystallite size, and the average microstrain of the samples.

Sample	Lattice Parameters		Crystallite Size, [nm]	Microstrain, [%]
	a, [Å]	c, [Å]		
TiO_2 MW (450 °C)	3.788359 ± 0.000278	9.508230 ± 0.000739	16	0.57 ± 0.16
TiO_2−Cu 2.0% MW	3.788145 ± 0.000340	9.504234 ± 0.000896	14	0.65 ± 0.19
TiO_2−Zn 2.0% MW	3.790948 ± 0.000383	9.500206 ± 0.001015	12	0.75 ± 0.22
TiO_2, anatase (ICDD 21-1272)	3.7850	9.5140	-	-

According to the calculated values for the lattice parameters, no differences were noticed compared to the standard reference file (ICDD 21-1272), suggesting that Cu and Zn dopants probably substitute for Ti in the TiO_2 host lattice. The crystallite size was influenced by the doping cation; thus, the sizes are smaller by 2 nm for Cu and 4 nm for Zn. The evolution in the mean crystallite size may be correlated with the increase in the lattice strain, where lattice strain is a measure of crystal defects, where the defects are generated by the larger ionic radius of Cu^{2+} (0.73 Å) and Zn^{2+} (0.74 Å) compared to that of Ti^{4+} (0.61 Å).

2.2.3. XRF Results

The presence of the dopant elements in the sample composition was investigated by X-ray fluorescence analysis. Table 4 lists the composition in terms of elements, as well as

oxides. We noticed that Cu and Zn oxides were detected in amounts close to the initial calculated composition. Other elements (C, S, Si or V) were detected as traces. Small differences compared to the initial composition could be determined by the washing procedure.

Table 4. Elemental composition of the analyzed samples.

Sample	Composition	Values	U.M.	Line
TiO_2−Zn 2.0% MW	Ti	57.9936	mass%	Ti−KA
	Zn	1.6021	mass%	Zn−KA
	O	39.0359	mass%	O−KA
	C, S, Si, V (traces)	1.6684	mass%	
	TiO_2	93.2240	mass%	Ti−KA
	ZnO	1.8994	mass%	Zn−KA
	C, S, Si, V oxides (traces)	4.8766	mass%	
TiO_2−Cu 2.0% MW	Ti	56.7392	mass%	Ti−KA
	Cu	1.6454	mass%	Cu−KA
	O	40.3301	mass%	O−KA
	C, Si, S (traces)	1.2	mass%	
	TiO_2	93.3325	mass%	Ti−KA
	CuO	2.0222	mass%	Cu−KA
	C, S, Si oxides (traces)	4.6453	mass%	

2.2.4. TEM/HRTEM/SAED Investigations

Figure 9 depicts the results of the TEM/HRTEM/SAED investigations for the thermally treated samples. Lower-magnification TEM images confirm that the quasispherical particles observed in the SEM images are aggregates of polyhedral primary nanoparticles that are nearly uniform in shape and size [70] (Figure 9a,d). Since individual nanoparticles were only spotted close to the aggregate surfaces, it is difficult to estimate the particle average size with any degree of accuracy. Nonetheless, a rough calculation shows that the values of these nanoparticles' diameters are in the 10–20 nm range, which is in agreement with the average crystallite sizes listed in Table 3. This demonstrates that the particles in question for both analyzed powders are single-crystal. In spite of their size, the nanoparticles exhibit a high crystallinity degree, regardless of the dopant, as shown by the long-range ordered fringes inside the nanoparticles revealed by the HRTEM images in Figure 9b,e and the well-defined dashed diffraction rings made up of bright spots of the SAED patterns (Figure 9c,f).

2.2.5. STEM/EDX Investigations

The Ti, O, and dopant species that make up the anatase solid solutions are exclusively present, according to the EDX spectra of the Cu- and Zn-doped TiO_2 powders, ruling out any contamination during the synthesis process (Figure 10).

Due to the consistent integration of the dopant into the host crystalline structure, the overall and elemental EDX maps (Figure 10b–d,f–h) recorded on the areas indicated by the STEM images of Figure 10a,e demonstrate a high compositional homogeneity of both powders. These results are consistent with the XRD data, revealing the presence of the single anatase phase and the absence of any segregation of any residual secondary phases.

2.2.6. XPS on the Thermally Treated Samples

XPS measurements were also performed on the treated samples and were analyzed in the same way; see Table 5 for the relevant parameters obtained from the deconvolutions. All the core-level spectra of interest are illustrated in Figures 11–14. The Cu 2p spectra show some additional peaks, which are satellites (peaks arising from various less-likely electron transitions). It can be observed that, in this case, there are some changes in the shape of the spectra, and the most significant one relates to the satellite peaks at ~945 eV and 967 eV, confirming the presence of the Cu(II) valence of Cu [67]; this can be assumed to

result from the preparation method, as the presence of this valence was not observed when the samples were synthesized only by the sol–gel process [35].

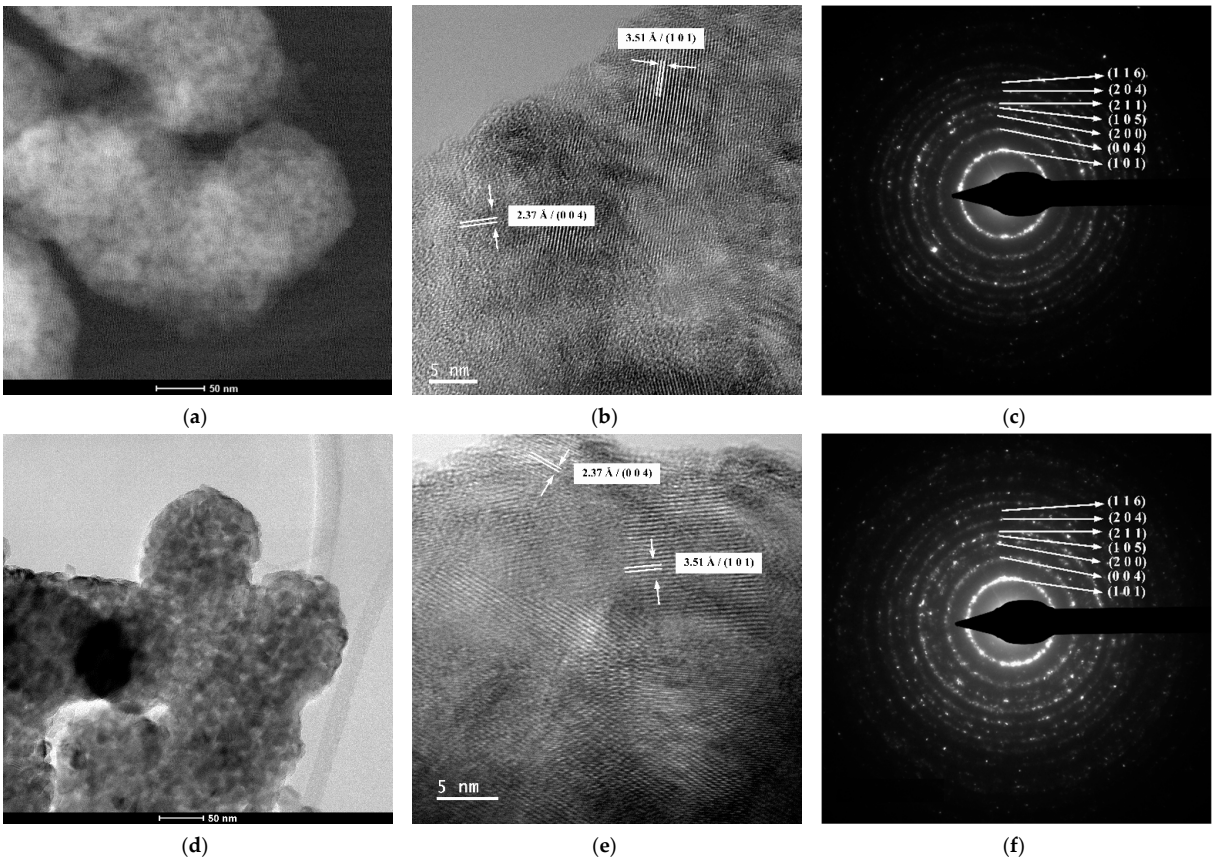

Figure 9. TEM images (**a**,**d**), HRTEM images (**b**,**e**), and SAED patterns (**c**,**f**) of the thermally treated samples: TiO_2−Cu 2.0% MW (**a**–**c**) and TiO_2−Zn 2.0% MW (**d**–**f**).

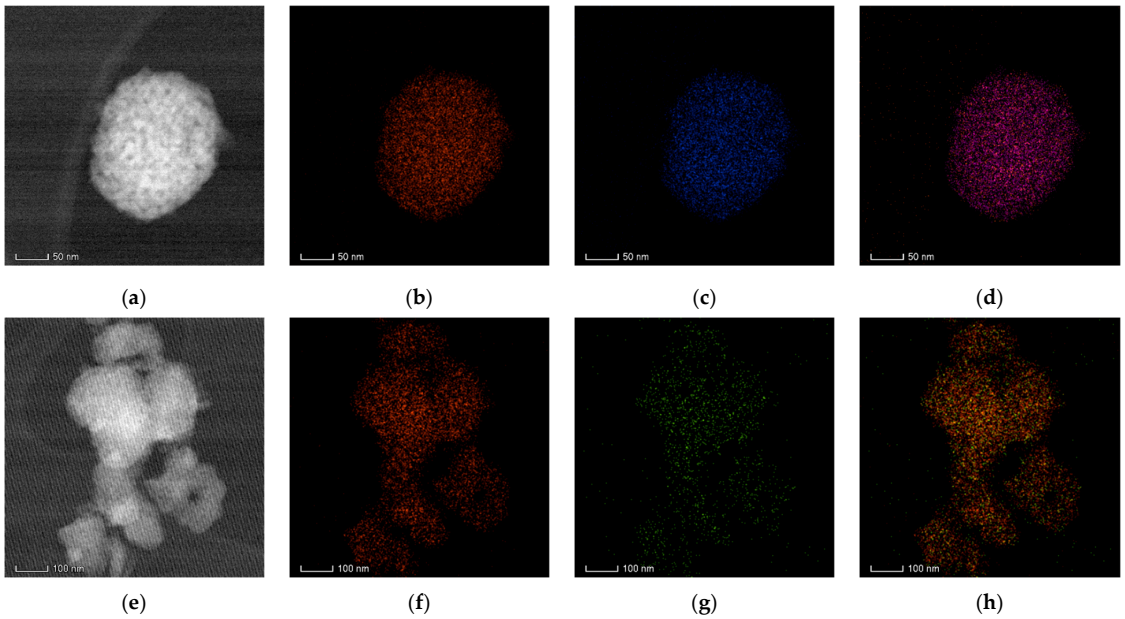

Figure 10. STEM image of TiO_2−Cu 2.0% MW (**a**) and TiO_2−Zn 2.0% MW (**e**) samples, EDX map of Ti in TiO_2−Cu 2.0% MW (**b**) and TiO_2−Zn 2.0% MW (**f**), Cu in TiO_2−Cu 2.0% MW (**c**), Zn in TiO_2−Zn 2.0% MW (**g**), Ti + Cu in TiO_2−Cu 2.0% MW (**d**), and Ti + Zn in TiO_2−Zn 2.0% MW (**h**).

Table 5. Binding energies (BE), atomic %, and attributions of the deconvolutions for the core levels for the treated samples.

	Element		BE (eV)	% at	Interpretation
TiO_2-Zn 2.0% TT (500 °C)	Ti $2p_{3/2}$	C1	458.7	24.1	Ti(IV) vol.
		C2	459.53	4.5	Ti(IV) surf.
				28.6	
	O 1s	C1	529.94	42.5	Ti(IV)
		C2	530.83	27.1	Ti(IV)+Zn(II)+cont
				69.6	
	Zn $2p_{3/2}$	C1	1022.39	1.8	Zn(II)
					$TiO_{2,43}$—Zn 1.8%
TiO_2-Cu 2.0% TT (500 °C)	Ti 2p	C1	458.6	16.7	Ti(IV)
		C2	460	4.2	TiO_x
		C3	461.4	3.1	Ti
				24.0	
	O 1s	C1	529.79	31.5	Ti(IV)
		C2	530.71	21.8	TiO_x+ organics
		C3	532.61	20.8	TiO_x/OH groups [71]
				74,1	
	Cu $2p_{3/2}$	C1	936.3	1,9	Cu(II)
					$TiO_{2,22}$—Cu 1.9%

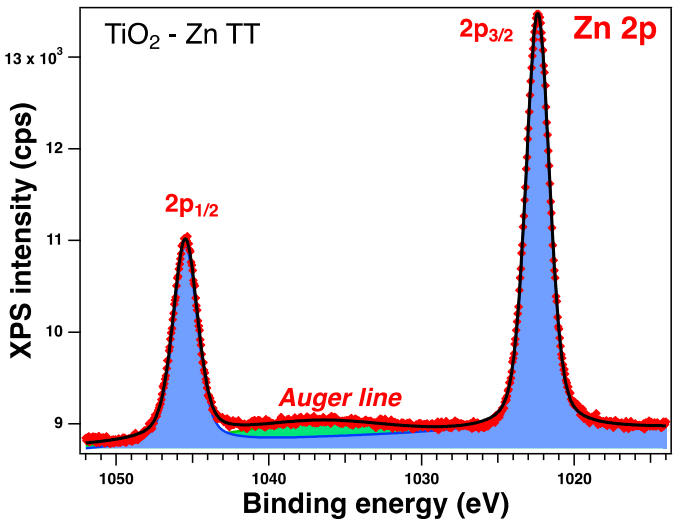

Figure 11. XPS spectra of the Zn 2p level of the thermally treated Zn-doped sample: red symbols for the experimental data, black line for the fit, blue line for C1, and green line for C2, which is an Auger peak.

2.2.7. UV-Vis Absorption Spectra

The optical properties of the synthesized powders were analyzed using UV−Vis spectroscopy; the absorption spectra are shown in Figure 15a. Both doped TiO_2 MW samples show an intense absorption band in the UV region (up to 350 nm) due to the electronic transitions O2p→Ti3d from the valence band (VB) to the conduction band (CB) of TiO_2 [72]. A red shift of absorption band was observed for the TiO_2−Cu 2.0% MW sample, due to the electron transition from O2p of TiO_2 to the Cu^{2+} d-states (400–550 nm) and due to

the d–d transitions of Cu^{2+} ions (600–800 nm) [73,74], indicating that doping TiO_2 MW with copper led to an increase in visible-light-absorption capacity of the synthesized material. For the TiO_2−Zn 2.0% MW sample, no absorption bands assigned to d–d transitions were observed, due to the complete electronic configuration of incorporated Zn^{2+} species [38].

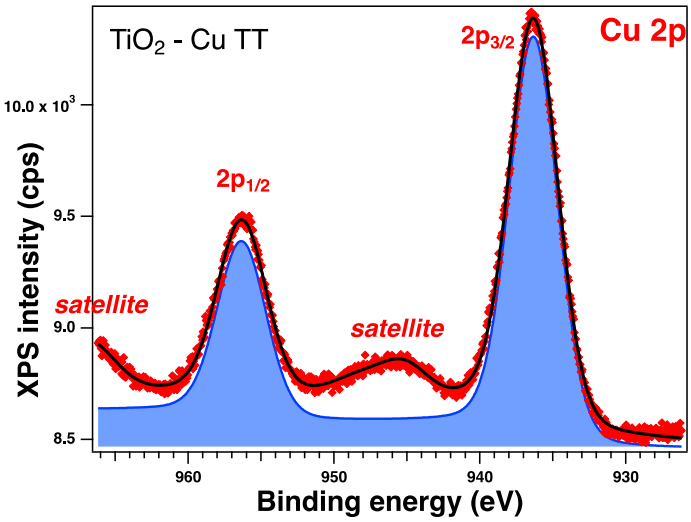

Figure 12. XPS spectra of Cu 2p level of the thermally treated Cu-doped sample: red symbols for the experimental data and black line for the fit with one component (blue line) and satellite peaks.

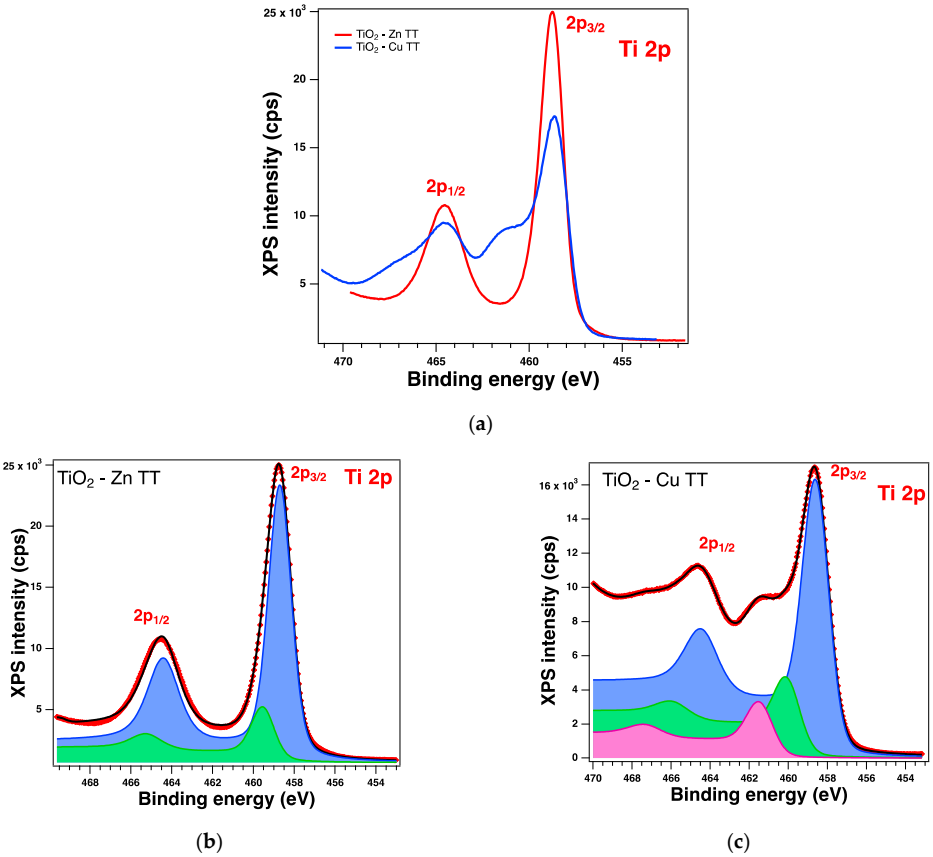

Figure 13. XPS spectra of the Ti 2p level for treated samples: (**a**) comparison of experimental data: red line for the Zn-doped samples and blue line for the Cu-doped samples, and (**b**,**c**) the fit and deconvolutions for the Zn and the Cu samples, respectively: red symbols for the experimental data overlayed with a black line, blue line for C1, green line for C2, and magenta line for C3 (for (**c**) only).

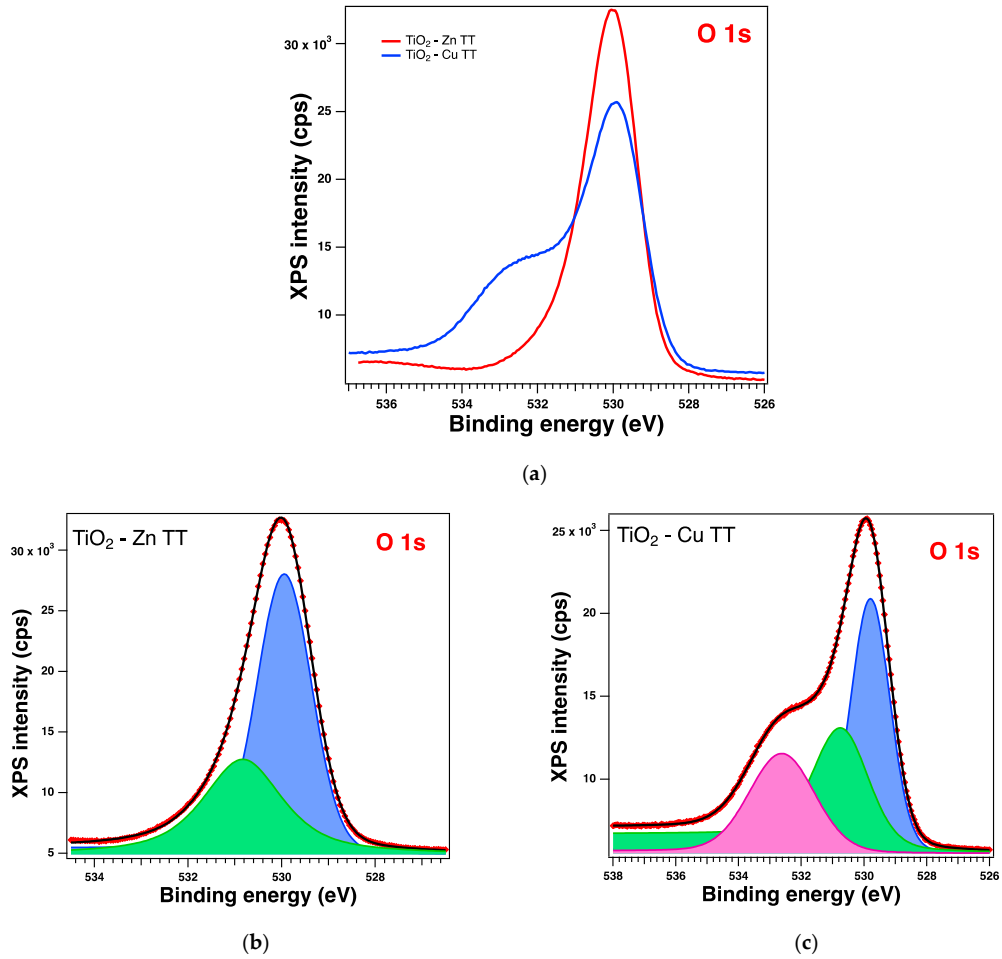

Figure 14. XPS spectra of the O 1s level for treated samples: (**a**) comparison of experimental data: red line for the Zn-doped samples and blue line for the Cu-doped samples, and (**b**,**c**) the fit and deconvolutions for the Zn and the Cu samples, respectively: red symbols for the experimental data overlayed with a black line, blue line for C1, green line for C2, and magenta line for C3 (for (**c**) only).

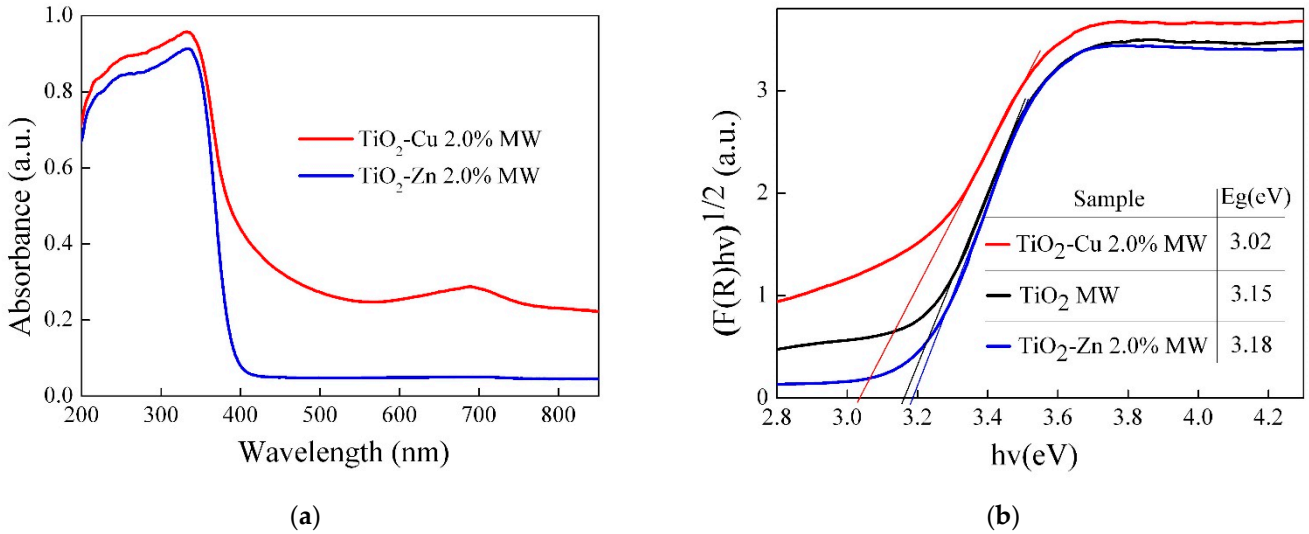

Figure 15. UV−Vis absorption spectra of (**a**) Cu/Zn-doped TiO_2 MW samples and (**b**) graphic representation of the Kubelka–Munk function for indirect transitions.

The indirect band gap energy of the samples was estimated using the Kubelka–Munk function by plotting $(F(R)*h\upsilon)^{1/2}$ versus photon energy hυ (eV). As shown in Figure 15b, by doping TiO_2 MW with copper, a narrowing of the band-gap energy was noticed, from 3.15 eV to 3.02 eV. It is probably due to the new electronic levels provided by the copper species under the conduction band of titania, available to accept the photoexcited electrons from the valence band of titania. The same behavior was not observed in the case of zinc doping, which led to a slight increase in the band-gap value from 3.15 eV to 3.18 eV. It is related to the completely filled $3d^{10}$ electronic configuration of Zn^{2+} species compared to Cu^{2+} with $3d^9$ configuration [38].

2.2.8. Photoluminescence Analysis

The photoluminescence spectra of the samples are illustrated in Figure 16. The intense signals recorded for the TiO_2 MW sample are due to the electron–hole repairing after the return of photoexcited electrons from the conduction band to the valence band of TiO_2. By modification with copper and zinc dopants, we noticed a quenching of the PL intensity of TiO_2 MW, indicating the suppression of e^-/h^+ pair recombination by providing interband levels. This explains the better photocatalytic activity visible for the TiO_2-Cu 2.0% MW sample with the lowest-intensity PL signal (Figure 17a).

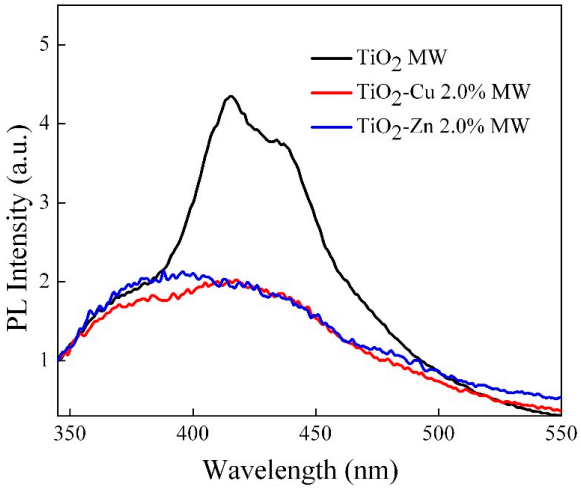

Figure 16. Photoluminescence spectra of doped and undoped TiO_2 nanopowders (λ_{exc} = 320 nm).

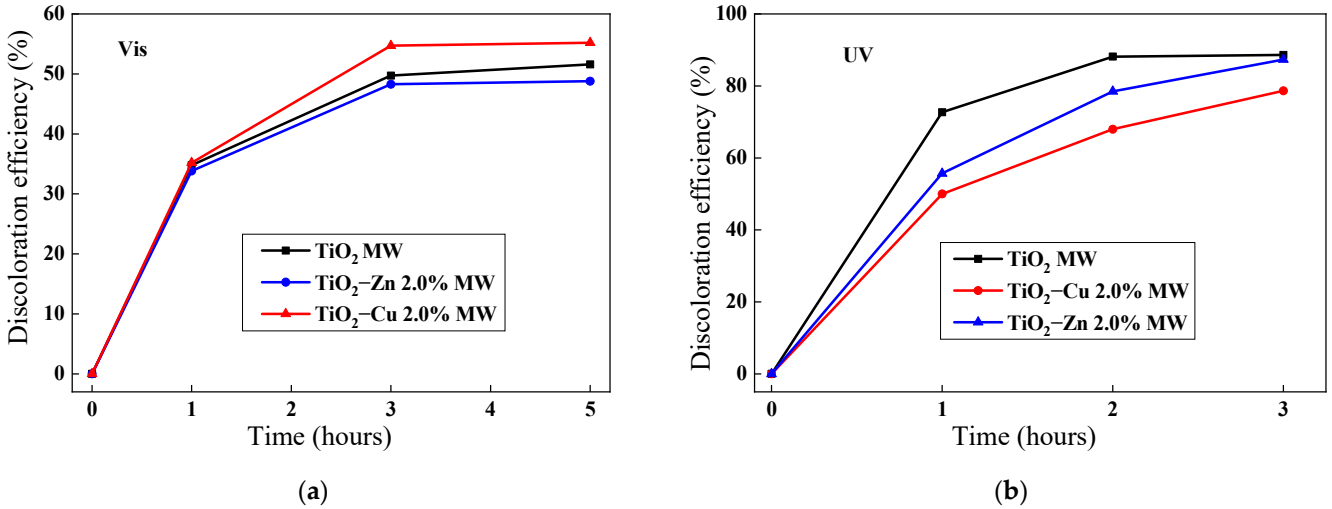

(**a**) (**b**)

Figure 17. Photocatalytic activity of the samples under (**a**) visible- and (**b**) UV-light irradiation.

2.2.9. Photocatalysis Investigation

The photocatalytic properties of the synthesized nanopowders were evaluated in the photocatalytic degradation of methyl-orange dye under visible- and UV-light irradiation (Figure 17). The best photocatalytic activity under visible-light irradiation (Figure 17a) was observed for the copper-doped TiO_2 sample, with a photocatalytic efficiency of 55.5% after 5 h of irradiation. This is related to the decrease in band-gap energy by doping with copper, which represents the minimum energy required for the electrons' excitation. The presence of features attributed to Cu^{2+} and surface hydroxyl groups in the XPS spectra (Figure 14) can contribute to this photocatalytic activity. Furthermore, the presence of surface hydroxyl groups suggested by the XPS spectra (Figure 14) could improve the photocatalytic activity [75,76]. Under UV-light irradiation (Figure 17b), the synthesized materials showed high photocatalytic activity, reaching almost 90% discoloration efficiency after 3 h of irradiation.

2.2.10. Identification of Reactive Species

In order to investigate the contribution of the main reactive oxygen species (ROS) to the MO degradation, the photocatalytic experiments were conducted in the presence of •OH, $\bullet O_2^-$, e^-, and h^+ scavengers. The results are illustrated in Figure 18a–c.

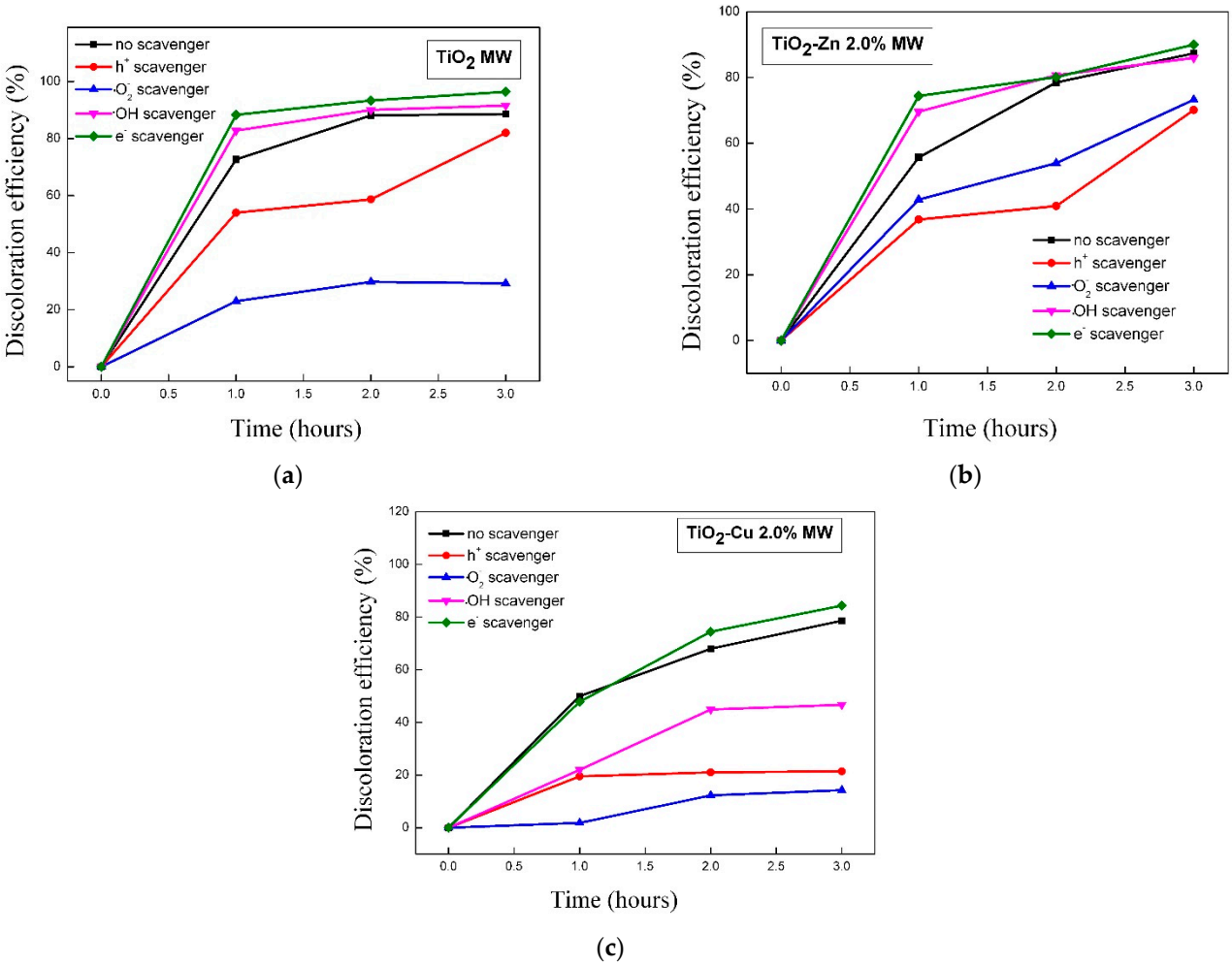

Figure 18. The effect of scavengers on the photocatalytic degradation of methyl orange under UV-light irradiation for (**a**) TiO_2 MW, (**b**) TiO_2-Zn MW, and (**c**) TiO_2 −Cu MW samples.

The order of reactive oxygen species contribution to MO degradation on TiO_2 MW and TiO_2-Cu 2.0% MW photocatalysts was as follows: $\bullet O_2^- > h^+ > \bullet OH > e^-$, indicating

that the photocatalytic degradation of MO dye mainly proceeded by the attack of superoxide radicals. The significant decrease in the photocatalytic performances noticed after p-benzoquinone addition (used as $\bullet O_2^-$ scavenger) suggests that $\bullet O_2^-$ species have a crucial role in the methyl-orange-degradation process by the two photocatalytic materials (Figure 18a,c).

In the case of the TiO_2-Zn 2.0% MW sample, the obtained results (Figure 18b) suggested that the photocatalytic degradation of MO was attributed especially to the holes, the order of the reactive species being the following: $h^+ > \bullet O_2^- > \bullet OH > e^-$.

An increase in the photocatalytic activity was observed when $AgNO_3$ was added into the reaction system as electron scavenger for all the samples, as a result of preventing e^-/h^+ recombination. In this way, there is a greater number of holes and electrons in the system, available to give rise to hydroxyl and superoxide radicals, respectively.

3. Conclusions

The different electron configurations of the Zn^{2+} and Cu^{2+} cations influenced the optical properties of the doped materials. By modifying TiO_2 MW with copper, it was possible to lower the band-gap energy to 3.02 eV, which led to an increase in the photocatalytic performance in the visible range. The experimental results showed that, under visible-light irradiation, the TiO_2-Cu 2.0% MW sample had a discoloration efficiency of 55% for MO dye after 5 h.

4. Materials and Methods

4.1. Materials

Cu- and Zn-doped TiO_2 nanopowders were obtained using the microwave-assisted sol–gel technique. Compositions with a TiO_2:CuO or TiO_2:ZnO molar percentage of 98:2 were selected. Except for the microwave irradiation, the preparation method and the reagents were previously described in Ref. [35]. The solution was exposed to microwave irradiation for 10 min at 200 W in an oven operating at a frequency of 2.45 GHz with a maximum power of 2000 W. To remove the water and organic residues and obtain crystallized nanometer-sized powders, the resulting oxide powder was filtered out of the solution, washed with distilled water to remove adsorbed compounds, dried, and then thermally treated at 500 °C in the air with a plateau of 1 h and a heating rate of 1 °C/min. The composition of the solutions and the experimental conditions used are shown in Table 6.

Table 6. The composition and the experimental conditions.

Sample	Precursors	Molar Ratio			pH Sol	Experimental Conditions	
		$\frac{ROH}{\sum precursor}$	$\frac{H_2O}{\sum precursor}$	$\frac{catalyst}{\sum precursor}$		T (°C)	t (min)
TiO_2-Cu 2.0% MW	$Ti(OC_4H_{10})_4$ + $Cu(NO_3)_2 \cdot 3H_2O$	36.5	3	0.003	10	60	10
TiO_2-Zn 2.0% MW	$Ti(OC_4H_{10})_4$ + $Zn(NO_3)_2 \cdot 6H_2O$	36.5	3	0.003	10	60	10

ROH = C_4H_9-OH.

The samples were denoted (TiO_2-Cu 2.0% MW) and (TiO_2-Zn 2.0%MW), and the thermally treated samples (TiO_2-Cu 2.0% MW-TT) and (TiO_2-Zn 2.0% MW-TT).

Our previous work [8] described the synthesis procedure for the TiO_2 MW sample (450 °C) (noted Ti-Bu-MW).

Figure 19 depicts a flowchart of the methodology used for sample preparation. Based on the TG/DTG/DTA results, the thermal treatment was determined.

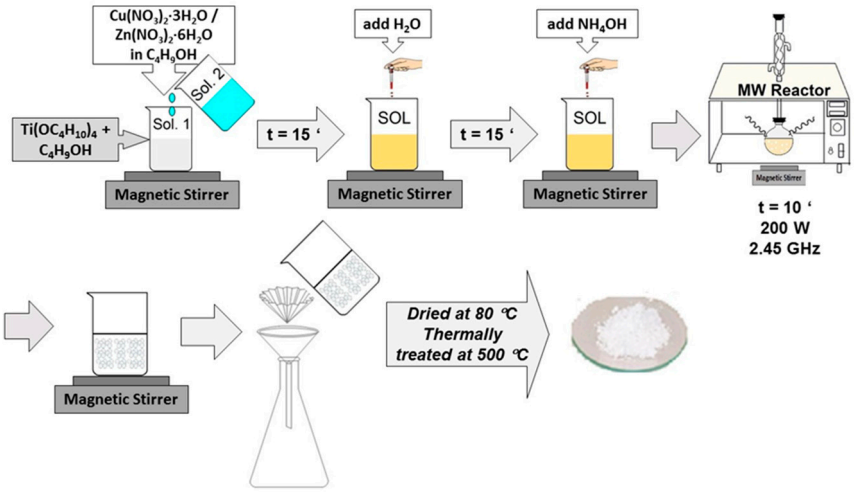

Figure 19. Flowchart of the methodology used for the sample preparation.

In order to investigate the contribution of the main important reactive oxygen species (ROS) to the photocatalytic degradation of MO, scavenger studies were conducted. For these experiments, commonly applied quencher molecules (0.1 mmol) were used for holes (potassium iodide, KI, Merck), electrons (silver nitrate, $AgNO_3$, Merck), hydroxyl (ethanol, C_2H_5OH, Merck), and superoxide radicals (p-benzoquinone, $C_6H_4O_2$, Merck).

4.2. Methods

Thermogravimetric and differential thermal analysis (TG/DTA), using Mettler Toledo TGA/SDTA 851^e (Greifensee, Switzerland) equipment, were used to assess the thermal behavior of the as-prepared samples in open Al_2O_3 crucibles and in flowing-air environments. The heating rate was 10 °C/min, and the maximum temperature was set to 1000 °C.

An FEI Quanta 3D FEG microscope (FEI, Brno, Czech Republic) operated at a 10 kV accelerating voltage was used to capture SEM micrographs. The uncoated specimens were placed on conductive carbon tape and scanned in high-vacuum mode.

The surface of the samples was investigated by the X-ray Photoelectron Spectroscopy (XPS) measurements performed in a SPECS Multimethod Surface Analysis System, with a PHOIBOS 150 hemispherical analyzer, using Al Kα (1486.74 eV) radiation produced by a monochromatic X-ray source XR50M at operating power of 250 W (12.5 kV × 20 mA). The base pressure in the analysis chamber was at least 1.1×10^{-8} mbar. For charge compensation, we used a SPECS FG−40 flood-gun device, using an electron beam of 0.1 mA and 1 eV energy. High-resolution core-level spectra (Ti 2p, O 1s, Zn 2p and Cu 2p) were recorded using medium-area-lens mode and a pass energy of 30 eV.

X-ray diffraction (XRD) patterns were recorded using a PANalytical Empyrean diffractometer (Malvern Panalytical, Malvern, UK) with Ni-filtered Cu K_α radiation (λ = 0.15406 Å). The equipment was set on theta–theta geometry, with a 1/4° divergence slit, 1/2° antiscatter slit, and 0.02° soller slit on the incident=beam side, and a 1/2° antiscatter slit mounted on PIXCel3D detector operating in 1D on the diffracted-beam side. The scan parameters were: range 10.0000–80.0107°, step size 0.0263°, and counting time per step 255 s. Phase analysis was performed using HighScorePlus 3.0.e software coupled with ICDD PDF4+ 2022 database. Determination of unit-cell parameters, average crystallite size, and microstrains was performed by Rietveld formalism, using a polynomial background with 4 parameters and a pseudo-Voigt function for line profiles.

Elements were analyzed using X-ray fluorescence (XRF). A Rigaku ZSX Primus II spectrometer (Rigaku Corp., Tokyo, Japan) with a 4.0 kW Xray Rh tube was used for the measurements. For data analysis, EZscan was combined with Rigaku SQX fundamental parameters software (standard less).

TEM/HRTEM/SAED investigations were carried out on the powders' morphology and crystallinity using a Thermo Fisher Scientific TITAN THEMIS Ultra High-Resolution

Electron Microscope (Hillsboro, OR, USA). The transmission-electron microscope was used in STEM (scanning transmission-electron microscopy) mode at 300 kV to acquire the EDX spectra and elemental maps, with a HAADF (high-angle annular dark-field) detector for imaging and a column windowless 4 Super EDX detector for elemental analysis.

An FLSP 920 spectrofluorometer was employed to record the photoluminescence spectra (PL) of the powders (Edinburgh Instruments, Livingston, UK). An Xe lamp was used as the excitation source, the excitation wavelength was 350 nm, and the spectra were recorded between 350 and 600 nm. Using a spectrofluorometer FluoroMax 4P (Horiba Jobin Yvon, Northampton, UK), the ability of the material to produce hydroxyl radicals in solution when exposed to light was assessed. This method employs terephthalic acid (TA) (5×10^{-4} M TA solution, prepared in aqueous NaOH solution with a concentration of 2×10^{-3} M), which interacts with the hydroxyl radicals generated by the photocatalytic materials during irradiation (λ_{exc} = 312 nm), yielding a highly fluorescent compound (2-hydroxyterephthalic acid).

The optical absorption spectra of powders were recorded using a JASCO V570 spectrophotometer (Tokyo, Japan). The photocatalytic activity of doped and undoped TiO_2 was measured in terms of the discoloration of methyl orange (MO) dye. Thus, 5 mg of photocatalyst was dispersed in 10 mL of MO aqueous solution (1×10^{-5} M), and further, the reaction mixture was stirred in the dark for 30 min in order to allow the adsorption of MO dye molecules on the photocatalyst surface. Then, the suspension stirred at the same constant speed was irradiated for a certain period of time (300 min in the case of UV irradiation and 180 min under visible-light irradiation) in a closed box with a UV−Vis lamp at certain specific wavelengths. At regular intervals of time, we took the same aliquots of MO solution and filtered them using syringe filters with a 0.45 μm pore size, and spectrophotometrically analyzed them in order to evaluate the progress of the photocatalytic reaction. The discoloration efficiency of the samples was evaluated using the absorbance value of the maximum peak (464 nm) that corresponds to the azo bond of MO dye recorded at the beginning of the reaction and after each time interval. In the case of ROS-scavenging experiments, the procedure was the same as in a photocatalytic test, except for the addition of scavengers (0.1 mmol) to the reaction mixture.

Author Contributions: Conceptualization, L.P., G.P. and S.P.; methodology, L.P., G.P. and S.P.; investigation, L.P., G.P., S.P., J.P.-C., S.V.P., A.B., N.G.A., R.M.C., V.-A.S. and B.Ş.V.; resources, L.P., N.G.A. and A.C.I.; writing—original draft preparation, L.P., G.P., S.P., J.P.-C., S.V.P., N.G.A., R.M.C. and A.C.I.; writing—review and editing, L.P., G.P., S.P., N.G.A. and A.C.I.; visualization, S.P. and L.P.; project administration, L.P., S.P. and A.C.I. All authors have read and agreed to the published version of the manuscript.

Funding: This research received no external funding.

Institutional Review Board Statement: Not applicable.

Informed Consent Statement: Not applicable.

Data Availability Statement: All data are available upon reasonable request from the authors.

Acknowledgments: This work was supported by the research program "Materials Science and Advanced Methods for Characterization" of the Institute of Physical Chemistry "Ilie Murgulescu", financed by the Romanian Academy.

Conflicts of Interest: The authors declare no conflict of interest.

References

1. Fujishima, A.; Rao, T.N.; Tryk, D.A. Titanium Dioxide Photocatalysis. *J. Photochem. Photobiol. C Photochem. Rev.* **2000**, *1*, 1–21. [CrossRef]
2. Bizarro, M.; Tapia-Rodríguez, M.A.; Ojeda, M.L.; Alonso, J.C.; Ortiz, A. Photocatalytic Activity Enhancement of TiO_2 Films by Micro and Nano-Structured Surface Modification. *Appl. Surf. Sci.* **2009**, *255*, 6274–6278. [CrossRef]
3. Dikici, T.; Demirci, S.; Tünçay, M.M.; Yildirim, B.K.; Kaya, N. Effect of Heating Rate on Structure, Morphology and Photocatalytic Properties of TiO_2 Particles: Thermal Kinetic and Thermodynamic Studies. *J. Sol-Gel Sci. Technol.* **2021**, *97*, 622–637. [CrossRef]

4. Cauqui, M.A.; Rodríguez-Izquierdo, J.M. Application of the Sol-Gel Methods to Catalyst Preparation. *J. Non-Cryst. Solids* **1992**, *147–148*, 724–738. [CrossRef]
5. Craciun, E.; Predoana, L.; Atkinson, I.; Jitaru, I.; Anghel, E.M.; Bratan, V.; Gifu, C.; Anastasescu, C.; Rusu, A.; Raditoiu, V.; et al. Fe^{3+}-Doped TiO_2 Nanopowders for Photocatalytic Mineralization of Oxalic Acid under Solar Light Irradiation. *J. Photochem. Photobiol. Chem.* **2018**, *356*, 18–28. [CrossRef]
6. Sun, Q.; Li, H.; Niu, B.; Hu, X.; Xu, C.; Zheng, S. Nano-TiO_2 Immobilized on Diatomite: Characterization and Photocatalytic Reactivity for Cu^{2+} Removal from Aqueous Solution. *Procedia Eng.* **2015**, *102*, 1935–1943. [CrossRef]
7. Zaharescu, M.; Predoana, L.; Pandele-Cusu, J. Thermal Analysis on Gels, Glasses, and Powders. In *Handbook of Sol-Gel Science and Technology: Processing, Characterization and Applications*; Klein, L., Aparicio, M., Jitianu, A., Eds.; Springer International Publishing: Cham, Switzerland, 2018; pp. 1833–1867. ISBN 978-3-319-32101-1.
8. Pandele-Cusu, J.; Petrescu, S.; Preda, S.; Petcu, G.; Ciobanu, M.; Predoana, L. Comparative Study of the TiO_2 Nanopowders Prepared from Different Precursors and Chemical Methods for Heterogeneous Photocatalysis Application. *J. Therm. Anal. Calorim.* **2022**, *147*, 13111–13124. [CrossRef]
9. Athar, T. Chapter 14—Metal Oxide Nanopowder. In *Emerging Nanotechnologies for Manufacturing*, 2nd ed.; Ahmed, W., Jackson, M.J., Eds.; Micro and Nano Technologies; William Andrew Publishing: Boston, MA, USA, 2015; pp. 343–401, ISBN 978-0-323-28990-0.
10. Athar, T. Chapter 17—Smart Precursors for Smart Nanoparticles. In *Emerging Nanotechnologies for Manufacturing*, 2nd ed.; Ahmed, W., Jackson, M.J., Eds.; Micro and Nano Technologies; William Andrew Publishing: Boston, MA, USA, 2015; pp. 444–538, ISBN 978-0-323-28990-0.
11. Chen, X.; Mao, S.S. Titanium Dioxide Nanomaterials: Synthesis, Properties, Modifications, and Applications. *Chem. Rev.* **2007**, *107*, 2891–2959. [CrossRef] [PubMed]
12. Singh, R.; Dutta, S. Synthesis and Characterization of Solar Photoactive TiO_2 Nanoparticles with Enhanced Structural and Optical Properties. *Adv. Powder Technol.* **2018**, *29*, 211–219. [CrossRef]
13. Stanciu, I.; Predoana, L.; Pandele-Cusu, J.; Preda, S.; Anastasescu, M.; Vojisavljevic, K.; Malic, B.; Zaharescu, M. Thermal Behaviour of the TiO_2-Based Gels Obtained by Microwave-Assisted Sol–Gel Method. *J. Therm. Anal. Calorim.* **2017**, *130*, 639–651. [CrossRef]
14. Predoana, L.; Stanciu, I.; Anastasescu, M.; Calderon-Moreno, J.M.; Stoica, M.; Preda, S.; Gartner, M.; Zaharescu, M. Structure and Properties of the V-Doped TiO_2 Thin Films Obtained by Sol–Gel and Microwave-Assisted Sol–Gel Method. *J. Sol-Gel Sci. Technol.* **2016**, *78*, 589–599. [CrossRef]
15. Vinogradov, A.V.; Vinogradov, V.V. Low-Temperature Sol–Gel Synthesis of Crystalline Materials. *RSC Adv.* **2014**, *4*, 45903–45919. [CrossRef]
16. Jongprateep, O.; Puranasamriddhi, R.; Palomas, J. Nanoparticulate Titanium Dioxide Synthesized by Sol–Gel and Solution Combustion Techniques. *Ceram. Int.* **2015**, *41*, S169–S173. [CrossRef]
17. Mehraz, S.; Kongsong, P.; Taleb, A.; Dokhane, N.; Sikong, L. Large Scale and Facile Synthesis of Sn Doped TiO_2 Aggregates Using Hydrothermal Synthesis. *Sol. Energy Mater. Sol. Cells* **2019**, *189*, 254–262. [CrossRef]
18. Kumar, S.G.; Rao, K.S.R.K. Polymorphic Phase Transition among the Titania Crystal Structures Using a Solution-Based Approach: From Precursor Chemistry to Nucleation Process. *Nanoscale* **2014**, *6*, 11574–11632. [CrossRef]
19. Fhoula, M.; Kallel, T.; Messaoud, M.; Dammak, M.; Cavalli, E. Morphological, Spectroscopic and Photocatalytic Properties of Eu^{3+}:TiO_2 Synthesized by Solid-State and Hydrothermal-Assisted Sol-Gel Processes. *Ceram. Int.* **2019**, *45*, 3675–3679. [CrossRef]
20. Lu, C.-W.; Cao, Y.; Li, H.; Webb, C.; Pan, W.-P. Synthesis of TiO_2 Based on Hydrothermal Methods Using Elevated Pressures and Microwave Conditions. *J. Therm. Anal. Calorim.* **2014**, *116*, 1241–1248. [CrossRef]
21. Bregadiolli, B.A.; Fernandes, S.L.; Graeff, C.F.D.O. Easy and Fast Preparation of TiO_2—Based Nanostructures Using Microwave Assisted Hydrothermal Synthesis. *Mater. Res.* **2017**, *20*, 912–919. [CrossRef]
22. Wei, X.; Cai, H.; Feng, Q.; Liu, Z.; Ma, D.; Chen, K.; Huang, Y. Synthesis of Co-Existing Phases Sn-TiO_2 Aerogel by Ultrasonic-Assisted Sol-Gel Method without Calcination. *Mater. Lett.* **2018**, *228*, 379–383. [CrossRef]
23. Simonsen, M.E.; Li, Z.; Søgaard, E.G. Influence of the OH Groups on the Photocatalytic Activity and Photoinduced Hydrophilicity of Microwave Assisted Sol–Gel TiO_2 Film. *Appl. Surf. Sci.* **2009**, *255*, 8054–8062. [CrossRef]
24. Andrade-Guel, M.; Díaz-Jiménez, L.; Cortés-Hernández, D.; Cabello-Alvarado, C.; Ávila-Orta, C.; Bartolo-Pérez, P.; Gamero-Melo, P. Microwave Assisted Sol–Gel Synthesis of Titanium Dioxide Using Hydrochloric and Acetic Acid as Catalysts. *Bol. Soc. Esp. Cerámica Vidr.* **2019**, *58*, 171–177. [CrossRef]
25. Reda, S.M.; Khairy, M.; Mousa, M.A. Photocatalytic Activity of Nitrogen and Copper Doped TiO_2 Nanoparticles Prepared by Microwave-Assisted Sol-Gel Process. *Arab. J. Chem.* **2020**, *13*, 86–95. [CrossRef]
26. Li, X.; Wang, L.; Lu, X. Preparation of Silver-Modified TiO_2 via Microwave-Assisted Method and Its Photocatalytic Activity for Toluene Degradation. *J. Hazard. Mater.* **2010**, *177*, 639–647. [CrossRef] [PubMed]
27. Tongon, W.; Chawengkijwanich, C.; Chiarakorn, S. Visible Light Responsive Ag/TiO_2/MCM-41 Nanocomposite Films Synthesized by a Microwave Assisted Sol–Gel Technique. *Superlattices Microstruct.* **2014**, *69*, 108–121. [CrossRef]
28. Baghbanzadeh, M.; Carbone, L.; Cozzoli, P.D.; Kappe, C.O. Microwave-Assisted Synthesis of Colloidal Inorganic Nanocrystals. *Angew. Chem. Int. Ed.* **2011**, *50*, 11312–11359. [CrossRef]
29. Brinker, C.J.; Scherer, G.W. CHAPTER 2—Hydrolysis and Condensation I: Nonsilicates. In *Sol-Gel Science*; Brinker, C.J., Scherer, G.W., Eds.; Academic Press: San Diego, CA, USA, 1990; pp. 20–95, ISBN 978-0-08-057103-4.

30. Basavarajappa, P.S.; Patil, S.B.; Ganganagappa, N.; Reddy, K.R.; Raghu, A.V.; Reddy, C.V. Recent Progress in Metal-Doped TiO_2, Non-Metal Doped/Codoped TiO_2 and TiO_2 Nanostructured Hybrids for Enhanced Photocatalysis. *Int. J. Hydrogen Energy* **2020**, *45*, 7764–7778. [CrossRef]
31. Nair, S.B.; John, K.A.; Joseph, J.A.; Babu, S.; Shinoj, V.K.; Remillard, S.K.; Shaji, S.; Philip, R.R. Fabrication and Characterization of Type-II Heterostructure n:In_2O_3/p:In-TiO_2 for Enhanced Photocatalytic Activity. *Phys. Status Solidi B* **2021**, *258*, 2000441. [CrossRef]
32. Bhanvase, B.A.; Shende, T.P.; Sonawane, S.H. A Review on Graphene–TiO_2 and Doped Graphene–TiO_2 Nanocomposite Photocatalyst for Water and Wastewater Treatment. *Environ. Technol. Rev.* **2017**, *6*, 1–14. [CrossRef]
33. Lettieri, S.; Pavone, M.; Fioravanti, A.; Santamaria Amato, L.; Maddalena, P. Charge Carrier Processes and Optical Properties in TiO_2 and TiO_2-Based Heterojunction Photocatalysts: A Review. *Materials* **2021**, *14*, 1645. [CrossRef]
34. Pham, T.-D.; Lee, B.-K. Cu Doped TiO_2/GF for Photocatalytic Disinfection of *Escherichia Coli* in Bioaerosols under Visible Light Irradiation: Application and Mechanism. *Appl. Surf. Sci.* **2014**, *296*, 15–23. [CrossRef]
35. Preda, S.; Pandele-Cușu, J.; Petrescu, S.V.; Ciobanu, E.M.; Petcu, G.; Culiță, D.C.; Apostol, N.G.; Costescu, R.M.; Raut, I.; Constantin, M.; et al. Photocatalytic and Antibacterial Properties of Doped TiO_2 Nanopowders Synthesized by Sol-Gel Method. *Gels* **2022**, *8*, 673. [CrossRef] [PubMed]
36. Bensouici, F.; Bououdina, M.; Dakhel, A.A.; Tala-Ighil, R.; Tounane, M.; Iratni, A.; Souier, T.; Liu, S.; Cai, W. Optical, Structural and Photocatalysis Properties of Cu-Doped TiO_2 Thin Films. *Appl. Surf. Sci.* **2017**, *395*, 110–116. [CrossRef]
37. Doustkhah, E.; Assadi, M.H.N.; Komaguchi, K.; Tsunoji, N.; Esmat, M.; Fukata, N.; Tomita, O.; Abe, R.; Ohtani, B.; Ide, Y. In Situ Blue Titania via Band Shape Engineering for Exceptional Solar H_2 Production in Rutile TiO_2. *Appl. Catal. B Environ.* **2021**, *297*, 120380. [CrossRef]
38. Chettah, W.; Barama, S.; Medjram, M.-S.; Selmane, M.; Montero, D.; Davidson, A.; Védrine, J.C. Anatase Titania Activated by Cu(II) or Zn(II) Nanoparticles for the Photooxidation of Methanol Assisted by Rhodamine-B. *Mater. Chem. Phys.* **2021**, *257*, 123714. [CrossRef]
39. Assadi, M.H.N.; Hanaor, D.A.H. The Effects of Copper Doping on Photocatalytic Activity at (101) Planes of Anatase TiO_2: A Theoretical Study. *Appl. Surf. Sci.* **2016**, *387*, 682–689. [CrossRef]
40. Maragatha, J.; Rajendran, S.; Endo, T.; Karuppuchamy, S. Microwave Synthesis of Metal Doped TiO_2 for Photocatalytic Applications. *J. Mater. Sci. Mater. Electron.* **2017**, *28*, 5281–5287. [CrossRef]
41. Garadkar, K.M.; Kadam, A.N.; Park, J. Microwave-Assisted Sol–Gel Synthesis Of Metal Oxide Nanomaterials. In *Handbook of Sol-Gel Science and Technology*; Klein, L., Aparicio, M., Jitianu, A., Eds.; Springer International Publishing: Cham, Switzerland, 2016; pp. 1–22, ISBN 978-3-319-19454-7.
42. Zhang, H.; Wang, M.; Xu, F. Generating Oxygen Vacancies in Cu^{2+} -Doped TiO_2 Hollow Spheres for Enhanced Photocatalytic Activity and Antimicrobial Activity. *Micro Nano Lett.* **2020**, *15*, 535–539. [CrossRef]
43. Lu, G.; Liu, X.; Zhang, P.; Xu, S.; Gao, Y.; Yu, S. Preparation and Photocatalytic Studies on Nanocomposites of 4-Hydroxylphenyl-Substituted Corrole/TiO_2 towards Methyl Orange Photodegradation. *ChemistrySelect* **2021**, *6*, 6841–6846. [CrossRef]
44. Rani, N.; Dehiya, B.S. Magnetically Recyclable Copper Doped Core-Shell Fe_3O_4@TiO_2@Cu Nanocomposites for Wastewater Remediation. *Environ. Technol.* **2022**, *43*, 4484–4492. [CrossRef] [PubMed]
45. Kanakaraju, D.; Ya, M.H.B.; Lim, Y.-C.; Pace, A. Combined Adsorption/Photocatalytic Dye Removal by Copper-Titania-Fly Ash Composite. *Surf. Interfaces* **2020**, *19*, 100534. [CrossRef]
46. Li, D.; Liang, Z.; Zhang, W.; Zhang, C. One-Step Synthesis of Cu/N Co-Doped TiO_2 Nanocomposites with Enhanced Photocatalytic Activities under Visible-Light Irradiation. *Micro Nano Lett.* **2021**, *16*, 573–581. [CrossRef]
47. Li, D.; Liang, Z.; Zhang, W.; Dai, S.; Zhang, C. Preparation and Photocatalytic Performance of TiO_2-RGO-CuO/Fe_2O_3 Ternary Composite Photocatalyst by Solvothermal Method. *Mater. Res. Express* **2021**, *8*, 015025. [CrossRef]
48. Kanakaraju, D.; Jasni, M.A.A.; Pace, A.; Ya, M.H. Enhanced Dye-Removal Performance of Cu-TiO_2-Fly Ash Composite by Optimized Adsorption and Photocatalytic Activity under Visible Light Irradiation. *Environ. Sci. Pollut. Res.* **2021**, *28*, 68834–68845. [CrossRef]
49. Xu, Q.; Li, E.; Zhao, R.; Liang, T.; Zhang, H.; Hu, W.; Zhang, N. Preparation of Organic Porous Materials-TiO_2/Cu Composite with Excellent Photocatalytic Degradation Performances toward Degradation of Organic Pollutants in Wastewater. *J. Polym. Res.* **2020**, *27*, 186. [CrossRef]
50. Hampel, B.; Pap, Z.; Sapi, A.; Szamosvolgyi, A.; Baia, L.; Hernadi, K. Application of TiO_2-Cu Composites in Photocatalytic Degradation Different Pollutants and Hydrogen Production. *Catalysts* **2020**, *10*, 85. [CrossRef]
51. Wu, M.-C.; Wu, P.-Y.; Lin, T.-H.; Lin, T.-F. Photocatalytic Performance of Cu-Doped TiO_2 Nanofibers Treated by the Hydrothermal Synthesis and Air-Thermal Treatment. *Appl. Surf. Sci.* **2018**, *430*, 390–398. [CrossRef]
52. Yang, M.; Huang, T.; Tang, N.; Ou, B.; Zhang, W. Structure and Catalytic Performance of Zn-Doped TiO_2 Film. *Pigment Resin Technol.* **2019**, *48*, 508–514. [CrossRef]
53. Tariq, M.K.; Riaz, A.; Khan, R.; Wajid, A.; Haq, H.; Javed, S.; Akram, M.A.; Islam, M. Comparative Study of Ag, Sn or Zn Doped TiO_2 Thin Films for Photocatalytic Degradation of Methylene Blue and Methyl Orange. *Mater. Res. Express* **2019**, *6*, 106435. [CrossRef]

54. Oladipo, G.O.; Akinlabi, A.K.; Alayande, S.O.; Msagati, T.A.M.; Nyoni, H.H.; Ogunyinka, O.O. Synthesis, Characterization, and Photocatalytic Activity of Silver and Zinc Co-Doped TiO_2 Nanoparticle for Photodegradation of Methyl Orange Dye in Aqueous Solution. *Can. J. Chem.* **2019**, *97*, 642–650. [CrossRef]
55. Wang, L.; Liu, S.; Wang, Z.; Zhou, Y.; Qin, Y.; Wang, Z.L. Piezotronic Effect Enhanced Photocatalysis in Strained Anisotropic ZnO/TiO_2 Nanoplatelets via Thermal Stress. *ACS Nano* **2016**, *10*, 2636–2643. [CrossRef]
56. Chen, C.; Wang, Z.; Ruan, S.; Zou, B.; Zhao, M.; Wu, F. Photocatalytic Degradation of C.I. Acid Orange 52 in the Presence of Zn-Doped TiO_2 Prepared by a Stearic Acid Gel Method. *Dyes Pigments* **2008**, *77*, 204–209. [CrossRef]
57. Xu, J.-C.; Shi, Y.-L.; Huang, J.-E.; Wang, B.; Li, H.-L. Doping Metal Ions Only onto the Catalyst Surface. *J. Mol. Catal. Chem.* **2004**, *219*, 351–355. [CrossRef]
58. Xu, J.-C.; Lu, M.; Guo, X.-Y.; Li, H.-L. Zinc Ions Surface-Doped Titanium Dioxide Nanotubes and Its Photocatalysis Activity for Degradation of Methyl Orange in Water. *J. Mol. Catal. Chem.* **2005**, *226*, 123–127. [CrossRef]
59. Golubko, N.V.; Yanovskaya, M.I.; Romm, I.P.; Ozerin, A.N. Hydrolysis of Titanium Alkoxides: Thermochemical, Electron Microscopy, Saxs Studies. *J. Sol-Gel Sci. Technol.* **2001**, *20*, 245–262. [CrossRef]
60. Chen, J.; Gao, L.; Huang, J.; Yan, D. Preparation of Nanosized Titania Powder via the Controlled Hydrolysis of Titanium Alkoxide. *J. Mater. Sci.* **1996**, *31*, 3497–3500. [CrossRef]
61. Siwińska-Stefańska, K.; Zdarta, J.; Paukszta, D.; Jesionowski, T. The Influence of Addition of a Catalyst and Chelating Agent on the Properties of Titanium Dioxide Synthesized via the Sol–Gel Method. *J. Sol-Gel Sci. Technol.* **2015**, *75*, 264–278. [CrossRef]
62. Simonsen, M.E.; Søgaard, E.G. Sol–Gel Reactions of Titanium Alkoxides and Water: Influence of PH and Alkoxy Group on Cluster Formation and Properties of the Resulting Products. *J. Sol-Gel Sci. Technol.* **2010**, *53*, 485–497. [CrossRef]
63. Zeng, M.; Uekawa, N.; Kojima, T.; Kakegawa, K. Synthesis of Titania Particles by Low-Temperature Hydrolysis Reaction of Titanium Alkoxide and Their Surface Properties. *J. Ceram. Soc. Jpn.* **2007**, *115*, 840–845. [CrossRef]
64. Teodorescu, C.M.; Esteva, J.M.; Karnatak, R.C.; Afif, A.E. An Approximation of the Voigt I Profile for the Fitting of Experimental X-Ray Absorption Data. *Nucl. Instrum. Methods Phys. Res. Sect. Accel. Spectrometers Detect. Assoc. Equip.* **1994**, *345*, 141–147. [CrossRef]
65. Wagner, C.D.; Davis, L.E.; Zeller, M.V.; Taylor, J.A.; Raymond, R.H.; Gale, L.H. Empirical Atomic Sensitivity Factors for Quantitative Analysis by Electron Spectroscopy for Chemical Analysis. *Surf. Interface Anal.* **1981**, *3*, 211–225. [CrossRef]
66. Naumkin, A.V.; Kraut-Vass, A.; Gaarenstroom, S.W.; Powell, C.J. *NIST X-ray Photoelectron Spectroscopy Database*; NIST Standard Reference Database Number 20, Version 4.1, Last Update to Data Content: 2012, (Retrieved 9 February 2023); National Institute of Standards and Technology: Gaithersburg, MD, USA, 2000; p. 20899. [CrossRef]
67. ThermoFisher Scientific XPS Database. Available online: https://www.Thermofisher.Com/Ro/En/Home/Materials-Science/Learning-Center/Periodic-Table/Transition-Metal/Copper.Html (accessed on 9 February 2023).
68. ThermoFisher Scientific XPS Database. Available online: https://www.Thermofisher.Com/Ro/En/Home/Materials-Science/Learning-Center/Periodic-Table/Transition-Metal/Titanium.Html (accessed on 9 February 2023).
69. Byrne, C.; Moran, L.; Hermosilla, D.; Merayo, N.; Blanco, Á.; Rhatigan, S.; Hinder, S.; Ganguly, P.; Nolan, M.; Pillai, S.C. Effect of Cu Doping on the Anatase-to-Rutile Phase Transition in TiO_2 Photocatalysts: Theory and Experiments. *Appl. Catal. B Environ.* **2019**, *246*, 266–276. [CrossRef]
70. Liao, Y.-T.; Huang, Y.-Y.; Chen, H.M.; Komaguchi, K.; Hou, C.-H.; Henzie, J.; Yamauchi, Y.; Ide, Y.; Wu, K.C.-W. Mesoporous TiO_2 Embedded with a Uniform Distribution of CuO Exhibit Enhanced Charge Separation and Photocatalytic Efficiency. *ACS Appl. Mater. Interfaces* **2017**, *9*, 42425–42429. [CrossRef] [PubMed]
71. Nawaz, R.; Kait, C.F.; Chia, H.Y.; Isa, M.H.; Huei, L.W. Glycerol-Mediated Facile Synthesis of Colored Titania Nanoparticles for Visible Light Photodegradation of Phenolic Compounds. *Nanomaterials* **2019**, *9*, 1586. [CrossRef] [PubMed]
72. Akel, S.; Boughaled, R.; Dillert, R.; El Azzouzi, M.; Bahnemann, D.W. UV/Vis Light Induced Degradation of Oxytetracycline Hydrochloride Mediated by Co-TiO_2 Nanoparticles. *Molecules* **2020**, *25*, 249. [CrossRef] [PubMed]
73. Choudhury, B.; Dey, M.; Choudhury, A. Shallow and Deep Trap Emission and Luminescence Quenching of TiO_2 Nanoparticles on Cu Doping. *Appl. Nanosci.* **2014**, *4*, 499–506. [CrossRef]
74. Esmat, M.; Doustkhah, E.; Abdelbar, M.; Tahawy, R.; El-Hosainy, H.; Abdelhameed, M.; Ide, Y.; Fukata, N. Structural Conversion of Cu-Titanate into Photoactive Plasmonic Cu-TiO_2 for H_2 Generation in Visible Light. *ACS Sustain. Chem. Eng.* **2022**, *10*, 4143–4151. [CrossRef]
75. Cui, T.; Su, Y.; Fu, X.; Zhu, Y.; Zhang, Y. The Key Role of Surface Hydroxyls on the Activity and Selectivity in Photocatalytic Degradation of Organic Pollutants and NO Removal. *J. Alloys Compd.* **2022**, *921*, 165931. [CrossRef]
76. An, N.; Zhao, Y.; Mao, Z.; Agrawal, D.K.; Wang, D. Microwave Modification of Surface Hydroxyl Density for g-C_3N_4 with Enhanced Photocatalytic Activity. *Mater. Res. Express* **2018**, *5*, 035502. [CrossRef]

Disclaimer/Publisher's Note: The statements, opinions and data contained in all publications are solely those of the individual author(s) and contributor(s) and not of MDPI and/or the editor(s). MDPI and/or the editor(s) disclaim responsibility for any injury to people or property resulting from any ideas, methods, instructions or products referred to in the content.